Elastic modelling of lattice distortions in concentrated random alloys

Bassem Sboui, David Rodney, Pierre-Antoine Geslin

Elastic modelling of lattice distortions in concentrated random alloys

Bassem Sboui[a,b,*], David Rodney[b,*], Pierre-Antoine Geslin[a,*]

[a] *Univ. Lyon, CNRS, INSA Lyon, Université Claude Bernard Lyon 1, MATEIS, UMR5510, 69100 Villeurbanne, France*
[b] *Univ. Lyon, CNRS, Université Claude Bernard Lyon 1, Institut Lumière Matière, UMR5306, 69622 Villeurbanne, France*

Abstract

Lattice distortions, i.e. small atomic displacements away from the average lattice, are linked to a number of functional and mechanical properties of concentrated metallic alloys, particularly their yield strength. Here we develop an elastic model of lattice distortions where every atom is modeled as an Eshelby inclusion in a homogeneous elastic matrix. Local environment effects are included by considering fluctuating anisotropic eigenstrain tensors associated to the inclusions. The model is tested on several concentrated alloys, face-centered cubic (FCC) AlMg and FeNiCr alloys, as well as a fictitious body-centered cubic (BCC) binary alloy to study systematically and independently the effects of a size and an elastic modulus mismatch between the constituents. The elastic model predicts lattice distortions well when the size and elastic modulus mismatches are typically less than 5% and 25%, respectively. Interestingly, we find that when the size mismatch is small, as in FeNiCr alloys, the lattice distortion is dominated by the fluctuations of the dilatational eigenstrains rather than their average value as often assumed in elastic models of concentrated alloys. Moreover, models usually assume homogeneous elastic constants, while the limit obtained here of 25% is often exceeded in concentrated alloys, particularly with a BCC structure.

Keywords: High entropy alloys, Elasticity, Lattice distortion,

1. Introduction

Concentrated single-phase solid solutions, including medium- and high-entropy alloys [1, 2], form a new class of materials that attract significant interest due to their exceptional functional and structural properties [3, 4]. In these alloys, atoms of different chemical natures are distributed at random on lattice sites, as schematically represented in Fig. 1, with possibly some short-range order as in the case of the NiCoCr alloy [5, 6].

In random alloys, the interactions between atoms with different bond strengths and different sizes induce atomic displacements away from the ideal lattice sites shown schematically in Fig. 1. These displacements are referred to as lattice distortions. The associated local strains and stresses are the source of the strengthening of solid solutions, as recognized early on in the seminal works of Fleisher [7] and Labusch [8], and revisited more recently for concentrated alloys [9, 10]. For a N-atom system, the magnitude of the lattice distortions can be characterized by the mean square atomic displacement (MSAD) defined as:

$$\langle u^2 \rangle = \frac{1}{N} \sum_{n=1}^{N} \|\boldsymbol{r_n} - \boldsymbol{r_n^0}\|^2, \tag{1}$$

where $\boldsymbol{r_n^0}$ and $\boldsymbol{r_n}$ denote respectively the position of the n$^{\text{th}}$ atom in the ideal lattice and in the distorted lattice. The quantity $\|\boldsymbol{r_n} - \boldsymbol{r_n^0}\|$ thus simply represents the dis-

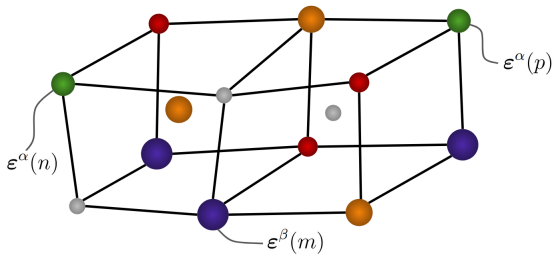

Figure 1: Illustration of lattice distortions in a random concentrated BCC alloy. To model these atomic displacements, we consider that an atom of type α located on site n is described by an Eshelby inclusion of eigenstrain tensor $\boldsymbol{\varepsilon}^{\alpha}(n)$.

*Corresponding authors
Email addresses: bassem.sboui@insa-lyon.fr (Bassem Sboui), david.rodney@univ-lyon1.fr (David Rodney), pierre-antoine.geslin@insa-lyon.fr (Pierre-Antoine Geslin)

placement of the n^{th} atom with respect to its reference lattice site. The amplitude of the MSAD is the subject of intense research (for reviews, see Refs. [11, 12]) because many properties of concentrated alloys, including but not limited to their yield strength, have been shown directly related to their lattice distortion [13–16].

Interestingly, so far, mostly the effect of the mismatch between atomic sizes has been studied, while the contrast between atomic bonds, related to the mismatch of elastic constants between constituents, is generally accepted as a weaker effect [9, 10]. Moreover, usually, only the effect of the average size mismatch is considered. The latter is quantified by the size mismatch parameter,

$$\delta = (\sum_i c_i(1 - r_i/\bar{r})^2)^{1/2}, \quad (2)$$

where the sum runs over the chemical elements, c_i is their concentration in the alloy, r_i their atomic radius and $\bar{r} = \sum_i c_i r_i$ the average radius [17]. Indeed, δ has proved a useful figure of merit to design alloys with high mechanical properties, for example in the case of TiNbHfTaZr alloys [18]. But δ does not tell the whole story. For instance, both Coury et al [19] and Lai et al [20] have shown that the shear modulus mismatch has a strong effect on the yield strength of body-centered cubic (BCC) concentrated alloys. We thus expect that the lattice distortions in these alloys are affected by both the size and elastic modulus mismatches.

Moreover, an average size mismatch does not capture the local variations of lattice distortions expected from the chemical complexity of concentrated random alloys. In metallic alloys, due to charge transfers [21, 22], the effective size of an atom depends on its local environment, which varies from atom to atom in concentrated random alloys. Asymmetric environments may also lead to local shear strains in addition to the size effect. Wide fluctuations of local strains are measured experimentally [23, 24] as well as in atomistic models [25, 26]. Moreover, fluctuations in bond strength, or force constants, are also evident in experiments [27, 28], although their potential effect has not been considered so far.

In this context, it appears valuable to develop models to estimate or even predict lattice distortions in concentrated alloys, including as many effects as possible. Several models have been developed [29–31] that rely on different elastic descriptions of the random alloys. Of particular interest here is the elastic model proposed by Geslin and Rodney [32, 33]. This model avoids the issue of distinguishing between solutes and solvents [11] by representing every atom in the alloy as an Eshelby inclusion embedded in an elastically homogeneous medium. Inclusions are defined as regions of space where a finite eigenstrain (also referred to as a transformation strain) is defined with respect to the surrounding matrix [34–36]. Solving for the elastic equilibrium yields the displacement field around the inclusion. The displacement of a given atom is then expressed by the sum of the displacements due to all surrounding atoms [37]. As a first step, the model only accounted for an average size mismatch effect by using strong simplifying assumptions: (i) only spherically symmetrical dilatational inclusions were considered, without anisotropic shear components, (ii) the effect of the local chemical environment, which induces fluctuations in the inclusion eigenstrains [38] was not included, each species having a given constant eigenstrain, (iii) the medium was considered elastically homogeneous and the potential effect of fluctuations of elastic constants was neglected. Discussing this last effect requires to distinguish elastic inclusions and inhomogeneities [36]. While inclusions denote a region with a finite eigenstrain tensor embedded in an elastic medium of homogeneous elastic constants, inhomogeneities denote a region characterized by elastic constants different from the surrounding medium.

Concentrated AlMg alloys that served as a model system in Refs. [32, 33] suit well the assumptions mentioned above because the size difference between both species is significant and depends only marginally on the local chemical environment, as confirmed by the present work. In addition, elastic constants of Al and Mg are comparable such that the elastic medium can be considered as homogeneous. However, applicability of the model to more complex alloys has proved limited.

In the present paper, we extend the elastic model introduced in Refs. [32, 33] to use the full eigenstrain tensor including dilatational and shear terms and to account for fluctuations of the eigenstrains due to the local chemical environment (Section 2). We test the model in Section 3 on several concentrated alloys modeled with embedded atom method (EAM) potentials, namely face-centered cubic (FCC) AlMg binary alloys and FeNiCr medium entropy alloys. We show that (1) shear terms are less important than dilatation terms and (2) fluctuations in the dilatational term may dominate the size effect. In order to retain an analytical model, we have not included elastic inhomogeneities. However, to evaluate systematically their potential effect, we study in Section 4 the properties of a fictitious body-centered cubic (BCC) binary alloy where the size and elastic mismatches between both species can be varied at will. Comparison between the model prediction and the atomistic calculations allows identifying when elastic inhomogeneities should be accounted for. We chose

to study in this section BCC concentrated alloys because they tend to exhibit larger size and elastic contrasts than FCC alloys [20, 39].

2. Elastic model for the mean-square atomic displacement

2.1. Elastic description of random alloys

We consider a random alloy, where N atoms of N_{elem} different species $(\alpha, \beta, \gamma..)$ are randomly distributed on a crystalline lattice. Randomness is modeled by using site occupancy variables $s_\alpha(n)$ that describes if an atom of type α occupies lattice site n. The statistical distributions of the occupancy variables are given by Bernoulli distributions:

$$\mathbb{P}[s_\alpha(n)] = \begin{cases} c_\alpha & \text{for} \quad s_\alpha(n) = 1 \\ 1 - c_\alpha & \text{for} \quad s_\alpha(n) = 0, \end{cases} \tag{3}$$

where c_α is the average concentration of element α in the alloy. This mathematical description of the random alloy is common to previous studies [32, 33, 37]. We consider that occupancy variables are not correlated between different lattice sites, meaning that we assume a fully random system without order. In the following, we will make use of the following relations for the statistical properties of the occupancy variables [32] :

$$\langle s_\alpha(n) s_\beta(m) \rangle = \begin{cases} c_\alpha & \text{if } \alpha = \beta \text{ and } n = m, \\ c_\alpha^2 & \text{if } \alpha = \beta \text{ and } n \neq m, \\ 0 & \text{if } \alpha \neq \beta \text{ and } n = m, \\ c_\alpha c_\beta & \text{if } \alpha \neq \beta \text{ and } n \neq m, \end{cases} \tag{4}$$

where $\langle ... \rangle$ denotes the statistical average over all possible configurations. The third equality stems from the fact that a given site cannot be occupied simultaneously by atoms of different types, such that one of the corresponding occupancy variables is necessarily zero. The fourth equality translates the fact that occupancy variables are not correlated on different lattice sites.

Atoms are described as elastic inclusions embedded in a continuous elastic medium. For simplicity reasons, the shape of these inclusions is considered spherical with a radius $a = (3v_{at}/4\pi)^{1/3}$, where v_{at} is the average atomic volume of the random alloy. As illustrated in Fig. 1, each inclusion is characterized by an eigenstrain tensor $[\boldsymbol{\varepsilon}]$ that describes the stress-free strain of the inclusion [35, 36].

In the following, tensors are written as vectors using Voigt notation:

$$\begin{aligned} \boldsymbol{\varepsilon}^\alpha(n) &= [\varepsilon_i^\alpha(n)]_{i\in\{1..6\}} \\ &= [\varepsilon_{11}^\alpha(n), \varepsilon_{22}^\alpha(n), \varepsilon_{33}^\alpha(n), \varepsilon_{23}^\alpha(n), \varepsilon_{13}^\alpha(n), \varepsilon_{12}^\alpha(n)]. \end{aligned} \tag{5}$$

As initially pointed out by Varvenne et al. [10], the size of an atom can vary depending on the chemical environment (see also Fig. 2). We will therefore consider that the components of the eigenstrain tensor associated with a given element are random variables described by normal distributions. Additionally, it is convenient to consider that the reference frame used to define the eigenstrains is the average alloy, such that for any component of the tensor, the eigenstrain averaged over lattice sites and realizations is 0:

$$\left\langle \sum_{n=1}^{N} \sum_{\alpha=1}^{N_{\text{elem}}} s_\alpha(n) \varepsilon_i^\alpha(n) \right\rangle = 0, \tag{6}$$

which reduces to:

$$\sum_{\alpha}^{N_{\text{elem}}} c_\alpha \langle \varepsilon_i^\alpha \rangle = 0. \tag{7}$$

Here we used the fact that the occupancy variable and atomic eigenstrains of a given site n are statistically independent. Indeed, the fluctuations of the eigenstrain at a site n depend on the occupancy of the surrounding sites ($s_\alpha(m)$ with $m \neq n$) but not on the occupancy of site n itself ($s_\alpha(n)$).

We consider that the eigenstrains are defined with respect to the canonical basis $(\boldsymbol{e_1}, \boldsymbol{e_2}, \boldsymbol{e_3})$ of cubic crystalline structures (FCC or BCC), such that we can take advantage of the high symmetry of the lattice to deduce relations on the statistical distributions. In particular, the axes $\boldsymbol{e_1}$, $\boldsymbol{e_2}$ and $\boldsymbol{e_3}$ are indistinguishable, such that the statistical distributions of the diagonal components ε_1^α, ε_2^α and ε_3^α are the same. We will denote their average and standard deviation by ε_d^α and σ_d^α respectively. In addition, we will account for the fact that two different diagonal terms ε_i and ε_j may be correlated. The symmetry of the structure imposes that this correlation is the same for all pairs of diagonal components and is defined with the following Pearson correlation parameter bounded between -1 and 1:

$$\rho_d^\alpha = \frac{\text{cov}(\varepsilon_i^\alpha, \varepsilon_j^\alpha)}{(\sigma_d^\alpha)^2} \quad \text{for} \quad i, j \leq 3 \text{ and } i \neq j \tag{8}$$

Symmetry arguments can also be used to clarify the statistical distributions of the shear components. If a

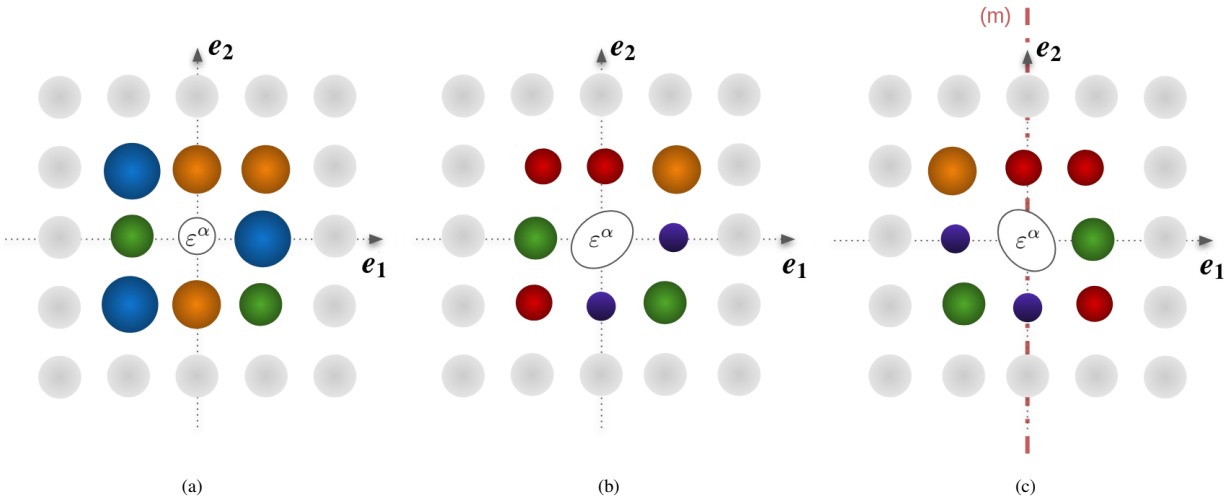

Figure 2: Illustration of the effect of the local chemical environment on the atomic eigenstrains.

specific environment leads for example to a shear eigenstrain ε_6, the mirror symmetry of this environment with respect to the plane of normal $\boldsymbol{e_1}$ will result in a shear eigenstrain $-\varepsilon_6$ (see schematics in Fig. 2.b-c). Since both environments have the same probability of occurrence, the statistical distribution of this shear component is symmetrical and its average is 0. In addition, since the axes $\boldsymbol{e_1}$, $\boldsymbol{e_2}$, and $\boldsymbol{e_3}$ are equivalent, the statistical distributions of the three shear components are necessarily the same. We note σ_s^α the standard deviation of the shear components associated with element α.

Symmetry arguments can also be used to show that the covariance between two shear components is zero. If a given environment leads to shear components $\varepsilon_4^\alpha, \varepsilon_5^\alpha$, a mirror symmetry with respect to the plane of normal $\boldsymbol{e_1}$ leads to shear components ε_4^α and $-\varepsilon_5^\alpha$, and therefore $\langle \varepsilon_4^\alpha \varepsilon_5^\alpha \rangle = 0$. Similar symmetry arguments can be used to show that the covariance between diagonal and shear components is also equal to zero.

The following equation summarizes the above considerations:

$$\langle \varepsilon_i^\alpha \varepsilon_j^\alpha \rangle = \begin{cases} (\varepsilon_d^\alpha)^2 + (\sigma_d^\alpha)^2 & \text{for} \quad i = j \leq 3 \\ (\varepsilon_d^\alpha)^2 + \rho_d^\alpha (\sigma_d^\alpha)^2 & \text{for} \quad i \neq j \text{ and } i, j \leq 3 \\ (\sigma_s^\alpha)^2 & \text{for} \quad i = j \geq 4 \\ 0 & \text{for} \quad i \neq j \text{ and } i \geq 4 \end{cases} \tag{9}$$

2.2. Mean-square atomic displacement

We assume that the elastic medium is homogeneous and isotropic, characterized by a shear modulus μ and Poisson's ratio ν. In such a medium, the displacement field around a spherical elastic inclusion is known analytically [35, 40]. In particular, the displacement field $u_k(\boldsymbol{r})$ along a specific direction k of the canonical basis is written as:

$$u_k(\boldsymbol{r}) = \sum_{i=1}^{6} \varepsilon_i^\alpha f_{ik}(\boldsymbol{r}), \tag{10}$$

with $f_{ik}(\boldsymbol{r})$ known analytical functions (see Appendix A). The validity of this elastic description of atomistic systems is tested in Appendix B where the displacement field around an atom characterized by a misfitting volume is successfully compared to the elastic solution of Eq. (10).

Based on the principle of superposition of linear elasticity [36], the displacement of an atom (arbitrarily located at the origin) in direction k is expressed as the sum of displacements due to all the atoms in the system:

$$u_k = -\sum_{n=1}^{N} \sum_{\alpha=1}^{N_{\text{elem}}} \sum_{i=1}^{6} s_\alpha(n) \varepsilon_i^\alpha(n) f_{ik}(\boldsymbol{R_n}), \tag{11}$$

where the first sum runs over all the lattice sites of the cubic crystalline lattice located at positions $\boldsymbol{R_n}$, the second sum runs over the potential elements occupying the sites and the third sum runs over the components of the eigenstrain tensor.

The displacement u_k is a random variable that depends on the realization, i.e. on the specific value of the occupancy variables $s_\alpha(n)$. Considering all possible realizations, it is apparent that the average of this displacement, with regard to the average alloy, is zero. On

the other hand, the variance is non-zero and is expressed as:

$$\langle u_k^2 \rangle = \left\langle \sum_{n,m}^{N} \sum_{\alpha,\beta}^{N_{\text{elem}}} \sum_{i,j}^{6} \varepsilon_i^\alpha(n)\varepsilon_j^\beta(m) s_\alpha(n) s_\beta(m) f_{ik}(\boldsymbol{R_n}) f_{jk}(\boldsymbol{R_m}) \right\rangle$$
$$= \sum_{n,m}^{N} \sum_{\alpha,\beta}^{N_{\text{elem}}} \sum_{i,j}^{6} \left\langle \varepsilon_i^\alpha(n)\varepsilon_j^\beta(m) s_\alpha(n) s_\beta(m) \right\rangle f_{ik}(\boldsymbol{R_n}) f_{jk}(\boldsymbol{R_m}). \tag{12}$$

As mentioned above, $\varepsilon_i^\alpha(n)$ is a priori correlated with $s_\alpha(m)$, for a lattice site m surrounding n, since the eigenstrain on a given site depends on its local environment. Following previous works [10], we make however the simplifying assumption that the fluctuations of the eigenstrains can be modeled without explicitly accounting for this dependence. We can then write

$$\left\langle \varepsilon_i^\alpha(n)\varepsilon_j^\beta(m) s_\alpha(n) s_\beta(m) \right\rangle = \langle \varepsilon_i^\alpha(n)\varepsilon_j^\beta(m) \rangle \langle s_\alpha(n) s_\beta(m) \rangle. \tag{13}$$

Using this assumption, and following previous works [10, 32, 37], we decompose Eq. (12) into the three sums:

$$\langle u_k^2 \rangle = \sum_{n,m}^{N} \sum_{\alpha,\beta}^{N_{\text{elem}}} \sum_{i,j}^{6} \langle \varepsilon_i^\alpha(n)\varepsilon_j^\beta(m) \rangle \langle s_\alpha(n) s_\beta(m) \rangle f_{ik}(\boldsymbol{R_n}) f_{jk}(\boldsymbol{R_m}) \tag{14}$$
$$= \underbrace{\sum_{n}^{N} \sum_{\alpha}^{N_{\text{elem}}} \sum_{i,j}^{6} \langle \varepsilon_i^\alpha(n)\varepsilon_j^\beta(n) \rangle \langle s_\alpha(n) s_\beta(n) \rangle f_{ik}(\boldsymbol{R_n}) f_{jk}(\boldsymbol{R_n})}_{S_1}$$
$$+ \underbrace{\sum_{n}^{N} \sum_{\alpha,\beta\neq\alpha}^{N_{\text{elem}}} \sum_{i,j}^{6} \langle \varepsilon_i^\alpha(n)\varepsilon_j^\beta(n) \rangle \langle s_\alpha(n) s_\beta(n) \rangle f_{ik}(\boldsymbol{R_n}) f_{jk}(\boldsymbol{R_n})}_{S_2}$$
$$+ \underbrace{\sum_{n,m\neq n}^{N} \sum_{\alpha,\beta}^{N_{\text{elem}}} \sum_{i,j}^{6} \langle \varepsilon_i^\alpha(n)\varepsilon_j^\beta(m) \rangle \langle s_\alpha(n) s_\beta(n) \rangle f_{ik}(\boldsymbol{R_n}) f_{jk}(\boldsymbol{R_m})}_{S_3}.$$

Since a given lattice site cannot be occupied by two different atoms (see Eq. (4)) $S_2 = 0$. Also, using Eq. (4) again, S_3 can be written as:

$$S_3 = \sum_{n,m\neq n}^{N} \sum_{\alpha,\beta}^{N_{\text{elem}}} \sum_{i,j}^{6} \langle \varepsilon_i^\alpha(n)\varepsilon_j^\beta(m) \rangle c_\alpha c_\beta f_{ik}(\boldsymbol{R_n}) f_{jk}(\boldsymbol{R_m})$$
$$= \sum_{i,j}^{6} \sum_{\alpha}^{N_{\text{elem}}} c_\alpha \langle \varepsilon_i^\alpha \rangle \sum_{\beta}^{N_{\text{elem}}} c_\beta \langle \varepsilon_j^\beta \rangle \sum_{n,m\neq n}^{N} f_{ik}(\boldsymbol{R_n}) f_{jk}(\boldsymbol{R_m})$$
$$= 0, \tag{15}$$

because of the average alloy's condition expressed in Eq. (7). Thus, Eq. (14) reduces to:

$$\langle u_k^2 \rangle = S_1 = \sum_{n}^{N} \sum_{\alpha}^{N_{\text{elem}}} \sum_{i,j}^{6} \langle \varepsilon_i^\alpha(n)\varepsilon_j^\beta(n) \rangle c_\alpha f_{ik}(\boldsymbol{R_n}) f_{jk}(\boldsymbol{R_n}). \tag{16}$$

Using the relations between different components of the eigenstrain tensor summarized in Eq. (9), the above equation can be written as

$$\langle u_k^2 \rangle = \sum_{\alpha=1}^{N_{\text{elem}}} ((\varepsilon_d^\alpha)^2 + (\sigma_d^\alpha)^2) c_\alpha \sum_{n=1}^{N} \left(\sum_{i=1}^{3} f_{ik}(\boldsymbol{R_n}) \right)^2 \tag{17}$$
$$+ \sum_{\alpha=1}^{N_{\text{elem}}} 2(\sigma_d^\alpha)^2 (\rho_d^\alpha - 1) c_\alpha \sum_{n=1}^{N} \sum_{i<j}^{3} f_{ik}(\boldsymbol{R_n}) f_{jk}(\boldsymbol{R_n})$$
$$+ \sum_{\alpha=1}^{N_{\text{elem}}} (\sigma_s^\alpha)^2 c_\alpha \sum_{n=1}^{N} \sum_{i=4}^{6} f_{ik}^2(\boldsymbol{R_n}).$$

The last step consists in combining the three equivalent directions ($k = 1, 2, 3$) and replacing the functions $f_{ik}(\boldsymbol{R_n})$ by their analytical expressions obtained from Refs. [40, 41] and reported in Appendix A. Finally, the mean square displacement is expressed by the sum of three contributions, associated with isotropic dilatations, anisotropic eigenstrains, and shears:

$$
\begin{aligned}
\langle u^2 \rangle &= \langle u^2_{\text{iso}} \rangle + \langle u^2_{\text{aniso}} \rangle + \langle u^2_{\text{shear}} \rangle \\
&= \frac{v_{at}^2}{16\pi^2}\left(\frac{1+\nu}{1-\nu}\right)^2 \underbrace{\sum_{\alpha=1}^{N_{\text{elem}}} \left((\varepsilon_d^\alpha)^2 + (\sigma_d^\alpha)^2\right) c_\alpha}_{A} \sum_{n=1}^{N} \frac{1}{R_n^4} \\
&+ \left(\frac{3v_{at}}{8\pi(1-\nu)}\right)^2 \Bigg\{ \underbrace{\sum_{\alpha=1}^{N_{\text{elem}}} 2(\sigma_d^\alpha)^2(\rho_d^\alpha - 1) c_\alpha}_{B} \sum_{n=1}^{N} \Bigg({R'_n}^4 \left(\frac{a^4}{5R_n^{12}} - \frac{2a^2(19-20\nu)}{15R_n^{10}} - \frac{(8\nu-7)}{3R_n^8} \right) \\
&\qquad - \frac{3a^4}{25R_n^8} - \frac{2a^2(4\nu-5)}{15R_n^6} - \frac{(2\nu-1)(2\nu-7)}{9R_n^4} \Bigg) \\
&\quad + \underbrace{\sum_{\alpha=1}^{N_{\text{elem}}} (\sigma_s^\alpha)^2 c_\alpha}_{C} \sum_{n=1}^{N} \Bigg({R'_n}^4 \Big(\frac{a^4}{5R_n^{12}} - \frac{2a^2(19-20\nu)}{15R_n^{10}} - \frac{8\nu-7}{3R_n^8} \Big) \\
&\qquad + \frac{2a^4}{25R_n^8} - \frac{4a^2(2\nu-1)}{15R_n^6} + \frac{2(2\nu-1)^2}{9R_n^4} \Bigg) \quad \Bigg\},
\end{aligned}
\tag{18}
$$

where ν is the Poisson ratio of the alloy, a is the radius of the spherical inclusions, and $v_{at} = \frac{4}{3}\pi a^3$, the associated atomic volume. In addition, denoting (x_n, y_n, z_n) the coordinates of lattice vector $\boldsymbol{R_n}$, the quantities R_n and R'_n are respectively defined as:

$$
R_n = \sqrt{x_n^2 + y_n^2 + z_n^2} \quad \text{and} \quad R'_n = \sqrt{\frac{x_n^2 y_n^2 + x_n^2 z_n^2 + y_n^2 z_n^2}{x_n^2 + y_n^2 + z_n^2}}.
$$

The mean-square displacement is therefore defined as a function of material parameters and geometric sums running over the crystalline lattice. The specific values of these sums depends on the crystalline lattice (FCC or BCC) and are listed in Appendix C. These sums are computed in the limit of infinite lattices ($N \to \infty$), effectively yielding the MSAD in an infinite system. We note that, if we considered the limiting case where the eigenstrain tensor associated with each atom's type is isotropic and unique, $\sigma_d^\alpha = \sigma_s^\alpha = 0$ and Eq. (18) reduces to

$$
\langle u^2 \rangle = \frac{v_{at}^2}{16\pi^2}\left(\frac{1+\nu}{1-\nu}\right)^2 \sum_{\alpha=1}^{N_{\text{elem}}} (\varepsilon_d^\alpha)^2 c_\alpha \sum_{n=1}^{N} \frac{1}{R_n^4}, \tag{19}
$$

in accordance with previous work [32].

We note that we took advantage of the high symmetry of cubic structures (FCC or BCC) to simplify the analytical expressions. Applying the same approach to lower symmetry crystals (such as hexagonal close packing structures) is straightforward and would yield a similar (but lengthier) expression than Eq. (18).

Computing the MSAD in Eq. (18) requires evaluating the terms A, B, and C, which depend on the statistical properties of the atomic eigenstrain's distribution of each element. The average values ε_d^α can be calculated by computing the change of lattice spacing with respect to the composition of the alloy [32, 33]. However, the variance and covariance of the eigenstrains are not as straightforward to evaluate. To do so, we propose in the following section a method based on the relation between the atomic eigenstrains and the equilibrium shape of finite-sized cells.

2.3. Link between atomic eigenstrains and cell strains

2.3.1. Cell strain tensor

Let us consider a periodic cubic cell of length $l = l_x = l_y = l_z$ containing a lattice with N atomic sites. The sites are occupied by atoms of different species following the Bernoulli distribution defined in Eq. (3). We assume with no further restriction that the atoms interact through an energy function, which can be minimized with respect to the atomic positions and cell shape to obtain equilibrium configurations with zero average stresses. The cell may then have different dimensions in

the x, y, and z directions and it may also acquire shear strains represented by tilt parameters l_{xz}, l_{xz} and l_{yz}. The tilt factor l_{xz} is defined as shown in Fig. 3(a); l_{xy} and l_{yz} are defined analogously. In Fig. 3(a), the cell length of the reference gray alloy, $\langle l \rangle$, is obtained by averaging over a large number N_{sim} of relaxations of atomistic cells containing a few thousand atoms (see below). For the cubic lattices considered here, we have by symmetry $\langle l \rangle = \langle l_x \rangle = \langle l_y \rangle = \langle l_z \rangle$ and $\langle l_{xy} \rangle = \langle l_{xz} \rangle = \langle l_{yz} \rangle = 0$. Once the gray alloy is defined, we can compute for each equilibrium configuration of the random alloy the corresponding cell strain tensor $[\boldsymbol{\varepsilon}^{\text{cell}}]$ with diagonal and shear terms defined as:

$$\varepsilon_1^{\text{cell}} = \frac{l_x - \langle l \rangle}{\langle l \rangle} \quad \text{and} \quad \varepsilon_4^{\text{cell}} = \frac{l_{yz}}{2\langle l \rangle}, \tag{20}$$

and similar definitions for the other diagonal and shear terms.

2.3.2. *Fluctuations of the cell shape*

The equilibrium cell shapes of two realizations of the random alloy can be different for two reasons: (1) due to the random choice of the chemical nature of the atoms using Bernoulli distribution, the concentration of the different species in a cell can be different from the target average composition; after relaxation, the lengths of the cell will depend on its specific composition and (2) if we consider two different configurations with the exact same composition, the relaxed lengths will be equal only if the atomic eigenstrains are independent of the local environment, which is a priori not true. We show in the following how the fluctuations of the equilibrium cell shape are related to the statistics of the atomic eigenstrains, and how this relation can be used to compute the A, B, and C terms needed to evaluate Eq. (18).

Within linear elasticity, the components of the cell strain tensor are related to the atomic eigenstrains by:

$$\varepsilon_i^{\text{cell}} = \frac{1}{N} \sum_{n}^{N} \sum_{\alpha}^{N_{\text{elem}}} s_\alpha(n) \varepsilon_i^\alpha(n), \tag{21}$$

with a zero average since

$$\langle \varepsilon_i^{\text{cell}} \rangle = \frac{1}{N} \sum_{n}^{N} \sum_{\alpha}^{N_{\text{elem}}} c_\alpha \langle \varepsilon_i^\alpha \rangle = 0, \tag{22}$$

as a consequence of the reference to the average alloy and the fact that we consider occupancy variables and atomic eigenstrains to be independent. Turning to the variance of cell strains, we have:

$$(\sigma_i^{\text{cell}})^2 = \frac{1}{N^2} \sum_{n,m}^{N} \sum_{\alpha,\beta}^{N_{\text{elem}}} \left\langle s_\alpha(n) s_\beta(m) \varepsilon_i^\alpha(n) \varepsilon_i^\beta(m) \right\rangle. \tag{23}$$

Using again the independence between occupancy variables and eigenstrains, we have:

$$(\sigma_i^{\text{cell}})^2 = \frac{1}{N^2} \sum_{n,n}^{N} \sum_{\alpha,\beta}^{N_{\text{elem}}} \langle s_\alpha(n) s_\beta(m) \rangle \langle \varepsilon_i^\alpha(n) \varepsilon_i^\beta(m) \rangle. \tag{24}$$

Following the same steps as in Section 2.2, we obtain:

$$(\sigma_i^{\text{cell}})^2 = \frac{1}{N^2} \sum_{n}^{N} \sum_{\alpha}^{N_{\text{elem}}} \langle \varepsilon_i^\alpha(n)^2 \rangle c_\alpha. \tag{25}$$

Depending on the component (tensile or shear terms), the variance of the cell strains is expressed as:

$$(\sigma_i^{\text{cell}})^2 = \begin{cases} (\sigma_d^{\text{cell}})^2 = \dfrac{1}{N} \displaystyle\sum_{\alpha}^{N_{\text{elem}}} ((\varepsilon_d^\alpha)^2 + (\sigma_d^\alpha)^2) c_\alpha, & i \leq 3, \\ (\sigma_s^{\text{cell}})^2 = \dfrac{1}{N} \displaystyle\sum_{\alpha}^{N_{\text{elem}}} (\sigma_s^\alpha)^2 c_\alpha, & i > 3. \end{cases} \tag{26}$$

Thus, the terms A and C defined in Eq. (18) are directly related to the variance of the cell strains:

$$A = N(\sigma_d^{\text{cell}})^2 \qquad C = N(\sigma_s^{\text{cell}})^2. \tag{27}$$

Following the same approach, the covariance between the diagonal terms of the cell strain tensor (i.e for $i \neq j$ and $i, j \leq 3$) can be expressed as:

$$\begin{aligned} \langle \varepsilon_i^{\text{cell}} \varepsilon_j^{\text{cell}} \rangle &= \text{cov}(\varepsilon_i^{\text{cell}}, \varepsilon_j^{\text{cell}}) + \underbrace{\langle \varepsilon_i^{\text{cell}} \rangle \langle \varepsilon_j^{\text{cell}} \rangle}_{=0} \\ &= \frac{1}{N^2} \sum_{n,m}^{N} \sum_{\alpha,\beta}^{N_{\text{elem}}} \left\langle s_\alpha(n) s_\beta(m) \varepsilon_i^\alpha(n) \varepsilon_j^\beta(m) \right\rangle. \end{aligned} \tag{28}$$

As previously, we decompose Eq. (28) into three sums, eventually yielding:

$$\text{cov}(\varepsilon_i^{\text{cell}}, \varepsilon_j^{\text{cell}}) = \frac{1}{N} \sum_{\alpha=1}^{N_{\text{elem}}} c_\alpha ((\varepsilon_d^\alpha)^2 + \text{cov}(\varepsilon_i^\alpha, \varepsilon_j^\alpha)) \tag{29}$$

Combining Eqs. (26) and (29), B can be expressed as a function of the statistics of the cell strain :

$$\begin{aligned} B &= \sum_{\alpha=1}^{N_{\text{elem}}} 2(\text{cov}(\varepsilon_i^\alpha, \varepsilon_j^\alpha) - (\sigma_d^\alpha)^2) c_\alpha \\ &= 2N(\text{cov}(\varepsilon_i^{\text{cell}}, \varepsilon_j^{\text{cell}}) - (\sigma_d^{\text{cell}})^2) \qquad (30) \\ &= 2N(\sigma_d^{\text{cell}})^2 (\rho_d^{\text{cell}} - 1) \qquad (31) \end{aligned}$$

where $\rho_d^{\text{cell}} = \dfrac{\text{cov}(\varepsilon_i^{\text{cell}}, \varepsilon_j^{\text{cell}})}{(\sigma_d^{\text{cell}})^2}$ is the Pearson correlation coefficient between the dilatational cell strain components. To summarize, the terms A, B, and C of Eq. (18)

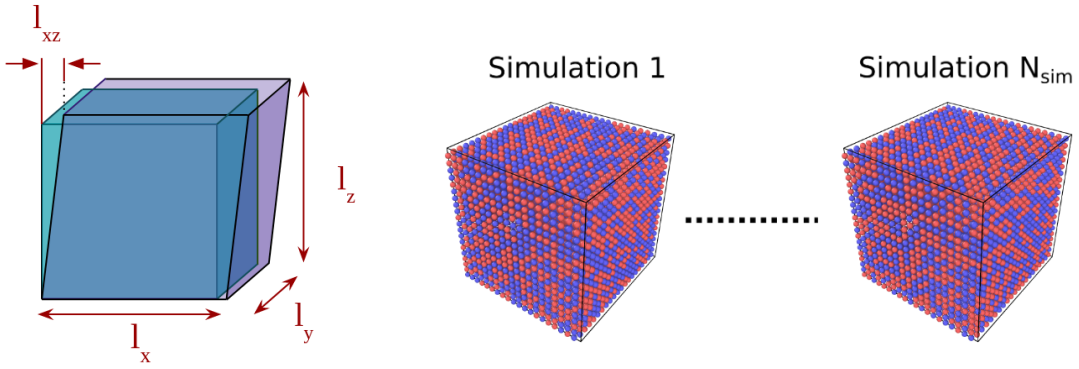

(a) (b)

Figure 3: (a) Sketch of a deformed cell: the blue box represents the cell averaged over all simulations, and the purple cell represents a configuration after relaxation. (b) Illustration of randomly distributed simulation cells for a binary alloy.

can be expressed as a function of the statistical properties of the cell strain tensor:

$$\begin{cases} A = \sum_\alpha \left((\varepsilon_d^\alpha)^2 + (\sigma_d^\alpha)^2 \right) c_\alpha & = N(\sigma_d^{\text{cell}})^2 \\ B = \sum_\alpha 2(\sigma_d^\alpha)^2(\rho_d^\alpha - 1)c_\alpha & = 2N(\sigma_d^{\text{cell}})^2(\rho_d^{\text{cell}} - 1) \\ C = \sum_\alpha (\sigma_s^\alpha)^2 c_\alpha & = N(\sigma_s^{\text{cell}})^2. \end{cases} \tag{32}$$

The cell strains are expressed as sums of independent random variables (see Eq. (21)). Applying the central limit theorem [42] establishes that they follow normal distributions. Estimating A, B and C thus requires to estimate the variance and covariance of the normal distributions, which is done from running a large number N_{sim} of independent atomistic simulations (see Fig. 3(b)). Because the distributions are Gaussian, standard errors on A, B and C decrease as $1/\sqrt{N_{sim}}$.

In the following, A, B and C are estimated from $N_{sim} = 4,000$ independent simulations containing $N_{at} = 4,000$ atoms in FCC systems and $N_{at} = 2,000$ in BCC systems. Using the fact that directions x, y, and z are equivalent in cubic systems, the variances $(\sigma_d^{\text{cell}})^2$, $(\sigma_s^{\text{cell}})^2$ and the covariance $\text{cov}(\varepsilon_i^{\text{cell}}, \varepsilon_j^{\text{cell}})$ are thus calculated from a collection of $12,000$ data points in FCC systems, $6,000$ in BCC systems. We have checked by direct calculations of A, B, and C in cells of increasing size that the estimates are well-converged, (see Appendix D for an example).

Therefore, analyzing the fluctuations of the cell shape of random alloys gives access to the statistics of the atomic eigenstrains, thus allowing us to evaluate Eq. (18) and to predict the MSAD. This elastically predicted MSAD can be compared to the atomistic MSAD to evaluate the accuracy of the elastic model as done in Sections 3 and 4 with different alloys.

3. Results - Environment-dependent anisotropic eigenstrains

3.1. Systems under study

In this section, we consider two alloys, AlMg, already used in Refs. [32, 33] to validate the isotropic version of the elastic model and FeNiCr, a medium-entropy alloy [43, 44]. Fe, Ni, and Cr are the main components of austenitic stainless steels, which are widely used in a range of applications. These components are also of interest for the study of multi-component concentrated alloys as they are present in many FCC high entropy alloys, including the historic Cantor alloy [2].

An $Al_{80}Mg_{20}$ alloy was modeled with the EAM potential of Ref. [45] as in previous work, where it was shown that the MSAD is dominated by the strong size mismatch between Al and Mg atoms. Therefore, we expect that the role of environment-dependent and non-diagonal eigenstrain components will be small compared to the size effect. Concerning FeNiCr, we employed the EAM potential of Bonny et al. [46]. All molecular statics simulations were performed with the Lammps package [47], with the use of two minimization algorithms: first, the Fast Inertial Relaxation Engine (FIRE) [48] allows for a fast relaxation with fixed boundary conditions. Second, the conjugate gradient (CG) also enables to relax the boundaries of the simulations cell to achieve zero pressure conditions. If the conjugate gradient fails to converge, additional iterations alternating FIRE and CG are performed until a relaxed configuration is reached. The convergence criterion for both algorithms is set as a maximum force of $f_{max} = 10^{-4}$ eV Å^{-1}.

3.2. Elastic MSAD

To evaluate the A, B, and C terms of Eq. (32) and predict the MSAD using the elastic model, we first estimate the average lattice parameter and elastic constants of the alloys using a cubic simulation cell containing $4,000$ atoms at the target composition. We note that the elastic anisotropy is quite pronounced in these alloys with Zener anisotropy coefficients ranging from 2 to 6 depending on composition. The isotropic shear modulus and Poisson's ratio are obtained using Bacon-Scattergood average [49, 50]. Second, we follow the methodology detailed in Section 2.3 to compute the A, B, and C terms from the fluctuations of the shape of 4,000-atom cells. As an example, Fig. 4 displays the histogram of the dilatational strain ε_d^{cell} obtained from 4000 random configurations of the equiatomic FeNiCr alloy. As expected from Eq. (21), this random variable follows a Gaussian distribution (shown in red).

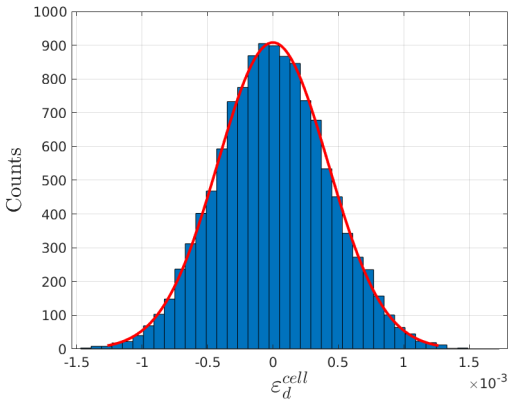

Figure 4: Distribution of the dilatational cell strain obtained from 4000 simulations for the equiatomic FeNiCr alloy. The red curve represents a Gaussian distribution.

For comparison, we also compute the term $\sum_\alpha c_\alpha(\varepsilon_d^\alpha)^2$, which corresponds to A without the environment-dependent fluctuations, by applying small changes to the composition around the alloy composition [10, 32, 51]. This corresponds to the initial isotropic version of the elastic model.

Tab. 1 lists the results for $Al_{80}Mg_{20}$, $Fe_{80}Ni_{20}$ and equiatomic FeNiCr alloys. In addition, Fig. 5 shows the correlations between $\varepsilon_1^{\text{cell}}$ and $\varepsilon_2^{\text{cell}}$ obtained from the $4,000$ atomistic calculations used for the statistics.

In the case of the $Al_{80}Mg_{20}$ alloy, $A \simeq \sum_\alpha c_\alpha(\varepsilon_d^\alpha)^2$, i.e. the fluctuations of the dilatational eigenstrain is negligible compared to its average. In addition, Fig. 5(a) shows a strong correlation between different eigenstrain components. For finite simulation cells, the composition of the cell changes slightly between realizations. As depicted by the color-coded plot, the strong correlation seen in Fig. 5(a) can be explained by these composition fluctuations: if the simulation cell contains more Mg atoms than the target composition, $\varepsilon_1^{\text{cell}}$ and $\varepsilon_2^{\text{cell}}$ are both larger than the average. Fig. 5(a) also confirms the weak effect of the environment on the dilatational eigenstrains: the values of $\varepsilon_1^{\text{cell}}$ and $\varepsilon_2^{\text{cell}}$ are primarily controlled by the composition of the alloy, and not by the atomic environments that change from one realization to the other. The strong correlation shown in Fig. 5(a) results in a value of $\rho_d^{cell} \simeq 1$ and, as a consequence, in a small value of $B \ll A$. Tab. 1 also reveals that $C \ll A$, showing that the role of the shear eigenstrains is negligible in this system. The MSAD is thus dominated by the average isotropic contribution, which explains why the isotropic model developed in Refs. [32, 33] worked well with this alloy.

The situation is strikingly different for the FeNi system. Fig. 5(b) shows that the values of the cell strains fluctuate greatly between two simulation cells with the same composition: even if simulation cells with less Ni tend to have larger values of $\varepsilon_1^{\text{cell}}$ and $\varepsilon_2^{\text{cell}}$, these quantities are not primarily controlled by the composition of the cell, but rather by the atomic environment that changes between cells of identical composition. This is confirmed in Tab. 1 where $A \gg \sum_\alpha c_\alpha(\varepsilon_d^\alpha)^2$. A is thus dominated by the fluctuation term in $Fe_{80}Ni_{20}$. Interestingly, the correlation between $\varepsilon_1^{\text{cell}}$ and $\varepsilon_2^{\text{cell}}$ is negative, which implies that the atomic eigenstrains associated with Fe and/or Ni atoms are anisotropic (e.g. with $\varepsilon_1 > 0$ and $\varepsilon_2, \varepsilon_3 < 0$), with an orientation that depends on the local environment. The importance of environment-dependent anisotropic eigenstrains for this system can be partly explained by the small size contrast between Fe and Ni atoms, resulting in a very small value of $\sum_\alpha c_\alpha(\varepsilon_d^\alpha)^2$ compared to the AlMg case (see Tab. 1).

The situation is similar for the equiatomic FeNiCr alloy where the size contrast between the different atoms is not prevalent. Fig. 5(c) shows that simulation cells with more Cr tend to be larger but again with a strong influence of the environment-dependent anisotropic eigenstrains. For both $Fe_{20}Ni_{80}$ and equiatomic FeNiCr alloys, the shear contribution $\langle u^2_{shear}\rangle$ is negligible, i.e. the off-diagonal terms of the atomic eigenstrain tensor remain small compared to the diagonal components. In addition, in both systems, $\langle u^2_{aniso}\rangle$ is smaller than $\langle u^2_{iso}\rangle$ but not negligible (about a factor 3 smaller), which translates the importance of accounting for the anisotropic effect to estimate the MSAD in these alloys. But primarily, the MSAD is dominated by the fluctuations of the isotropic dilatation for both alloys. These

	Eigenstrain terms ($\times 10^4$)				MSAD contributions ($\times 10^4$ Å^2)			
	$\sum_\alpha c_\alpha(\varepsilon_d^\alpha)^2$	A	B	C	$\langle u^2_{\text{iso}}\rangle$	$\langle u^2_{\text{aniso}}\rangle$	$\langle u^2_{\text{shear}}\rangle$	$\langle u^2\rangle$
$Al_{80}Mg_{20}$	21.8	23.1	-4.39	1.89	68.3	-1.72	1.54	68.1
$Fe_{80}Ni_{20}$	0.057	1.58	-4.41	0.0492	3.46	-1.37	0.032	2.12
FeNiCr	2.59	7.11	-14.1	0.296	18.1	-5.88	0.204	12.4

Table 1: Computed values of the $\sum_\alpha c_\alpha(\varepsilon_d^\alpha)^2$, A, B, and C terms for different alloys and corresponding contributions to the MSAD (see Eq. (18)). The last column corresponds to the total predicted MSAD: $\langle u^2\rangle = \langle u^2_{\text{iso}}\rangle + \langle u^2_{\text{aniso}}\rangle + \langle u^2_{\text{shear}}\rangle$.

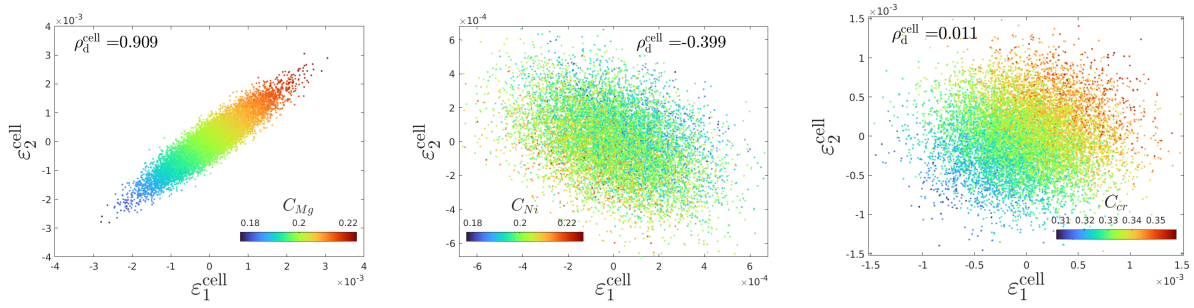

(a) (b) (c)

Figure 5: Cross-correlation between $\varepsilon_1^{\text{cell}}$ and $\varepsilon_2^{\text{cell}}$. Each dot represents a realization of a random alloy with average composition: (a) $Al_{80}Mg_{20}$ (b) $Fe_{80}Ni_{20}$ (c) equiatomic FeNiCr. The colors indicate the composition of the particular realization, showing the effect of this parameter on the measured strains. The overall cross-correlations are indicated by correlation coefficients ρ_d^{cell} on each graph.

results are in accordance with previous atomistic calculations [52] that show the wide distribution of misfit volumes of Ni and Cr in an austenitic steel.

3.3. Atomistic MSAD

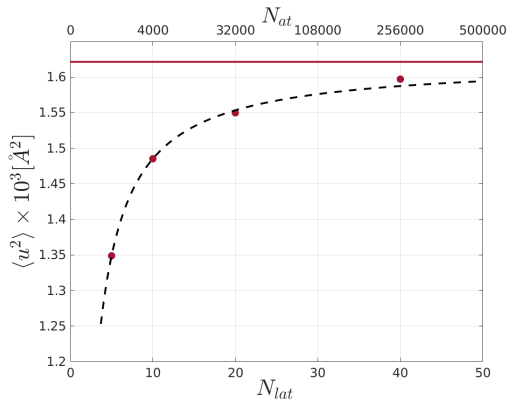

Figure 6: MSAD averaged over realizations of an equiatomic FeNiCr alloy as a function of the number of unit cells along a side of the cubic cell (N_{lat}) and the number of atoms in the cell (N_{at}). The dashed line represents a fitted function of the form $\langle u^2\rangle_\infty - \text{Cste}/N_{lat}$.

The atomistic MSAD of a given atomic system is computed using Eq. (1) after relaxing the atomic positions and the cell volume, using the average lattice of the relaxed cell as a reference. However, as pointed out in Ref. [33], the MSAD measured in a finite atomic system depends significantly on the system size due to the spatial correlations of the displacement field that display a long-range $1/r$ decay. Fig. 6 illustrates this effect in the case of an equiatomic FeNiCr alloy in cubic cells of increasing size. Here N_{lat} denotes the number of unit cells along the side of the cell and N_{at} is the corresponding number of atoms in the cell. For smaller simulation cells, the distribution of MSAD obtained with various configurations is wider, making it more difficult to estimate the average value. To compensate for this effect, the MSAD is averaged over an increasing number of configurations in smaller cell sizes ($N_{sim} = 4096, 512, 64, 8$ for $N_{lat} = 5, 10, 20, 40$). With these settings, the standard error on the estimated MSADs is independent of the cell size and the corresponding error bars are smaller than the symbol size in Fig. 6. As explained in Ref. [33], the MSAD converges with the size of the cell as $1/N_{lat}$. A simple non-linear fit shown as a dashed line in Fig. 6 enables to extract the MSAD for infinite systems, represented as a horizontal line.

We note that the smallest simulation cell considered here contains 500 atoms and underestimates the MSAD by 17%. Extrapolating to simulation cells of size $N_{lat} = 3$ containing 108 atoms typical of DFT studies [13, 21, 23, 24, 53, 54], the error is as high as 30%.

The slow convergence of the MSAD with the cell size contrasts with the rapid convergence of A, B, and C (see Appendix D). This is a consequence of the different nature of both quantities: the MSAD results from the long-range displacement fields of inclusions, explaining the slow convergence with the system size. On the other hand, estimating the parameters A, B, and C only requires having large enough cells to explore the statistically-relevant chemical environments.

We also note that the obtained value of $\langle u^2 \rangle_\infty = 1.63 \cdot 10^{-3}$ Å^2 found here for FeNiCr is within a factor 2 of $\langle u^2 \rangle_{exp} = 2.35 \cdot 10^{-3}$ Å^2 ($\pm 0.04 \cdot 10^{-3}$ Å^2) measured by X-Ray diffraction for an equiatomic FeNiCrMnCo alloy [13]. We expect that the presence of Mn and Co adds chemical complexity and therefore increases the value of the MSAD compared to the ternary FeNiCr alloy.

3.4. Comparison between elastic and atomistic MSADs for FeNiCr alloys

We now proceed with a comparison of the elastically predicted and atomistically computed MSAD in the case of FeNiCr alloys. Following the methodology detailed in section 3.3, we compute the value of the MSAD in the limit of an infinite system from atomistic simulations. We compare in Fig. 7 this direct measurement (blue symbols) to three predictions of the elastic model: the isotropic version of Ref. [32] (green squares), the current extended model (red squares) that includes all terms, i.e. non-diagonal eigenstrain components and environment-dependent contributions (red squares) and a simplified version of the model, which includes only the dilatational term and its fluctuations (dashed red curve, with $B = C = 0$ and $A \neq 0$). The difference between the green and dashed red curves is thus only due to the fluctuation of the isotropic dilatations.

As shown in Fig. 7, the full elastic model is close to the atomistic MSAD over the entire composition range, generally within 10 to 20% at most. This proves the capability of the elastic model to represent accurately lattice distortions in random concentrated alloys. This successful comparison also constitutes an *a posteriori* justification of the assumption embedded in Eq. (13) that consists in decorrelating environment statistics with occupancy variables.

Fig. 7 also reveals that the isotropic version of the elastic model underestimates significantly the atomistic MSAD. Comparing the prediction including (dashed red) or not (green) dilatational fluctuations, we see that the latter are very important and dominate over the size mismatch, as already observed in the previous section.

On the other hand, only incorporating the A term leads to an overestimation of the MSAD as compared to the direct atomistic calculations. Indeed, for this system, $B < 0$ for all compositions, which translates the fact that $\rho_d^\alpha < 1$ for some of the species. This reveals the presence of anisotropic eigenstrain components (with $\varepsilon_1 \neq \varepsilon_2 \neq \varepsilon_3$) with different orientations depending on the local environment. The influence of this type of environment-dependent anisotropic eigenstrain tensor can only be modeled accurately by accounting for the interplay between the A and B terms.

In the case of FeNiCr alloys, the main contribution to the MSAD comes from the fluctuations of the atomic eigenstrains. The role of these fluctuations, although discussed in the literature [10], is often neglected upon numerical application. We see however here that depending on the alloy considered, this term can play an important role and should not be neglected without justification.

The differences between elastic and atomistic MSAD can be attributed to factors that have been neglected to keep the model analytically tractable: (i) the role of chemical short-range interactions and (ii) the influence of the elastic medium anisotropy, which is pronounced in FeNiCr alloys.

The FeNiCr alloy presents the advantage of having relatively homogeneous elastic constants and can therefore be modeled as an elastically homogeneous medium. This assumption, which is central to apply our elastic model, is however not valid for all systems. We discuss this assumption in detail in the following.

4. Results - Role of heterogeneous elastic constants

Spatial heterogeneities of elastic constants are difficult to include in elastic models, which then require self-consistent formulations [36, 55]. However, there is clear experimental evidence of fluctuations in the atomic force constants of HEA [27, 28], which begs the question of the influence of the elastic constants' heterogeneities compared to the size mismatch. To answer this question, we propose a model potential for a fictitious BCC binary system, called $W - \widetilde{W}$. W denotes tungsten, with interactions described with the EAM potential developed by Marinica et al. [56] while $\widetilde{W}$ denotes a fictitious atom species. We will see how to modify the W potential to model $\widetilde{W}$ atoms that are bigger or smaller and/or stiffer or softer than W with controlled mismatches. We chose a BCC crystal because large elastic modulus mismatches are met in BCC concentrated solid solutions. Tungsten is also convenient because of its elastic isotropy. However, the approach detailed below applies to any element and any crystalline structure.

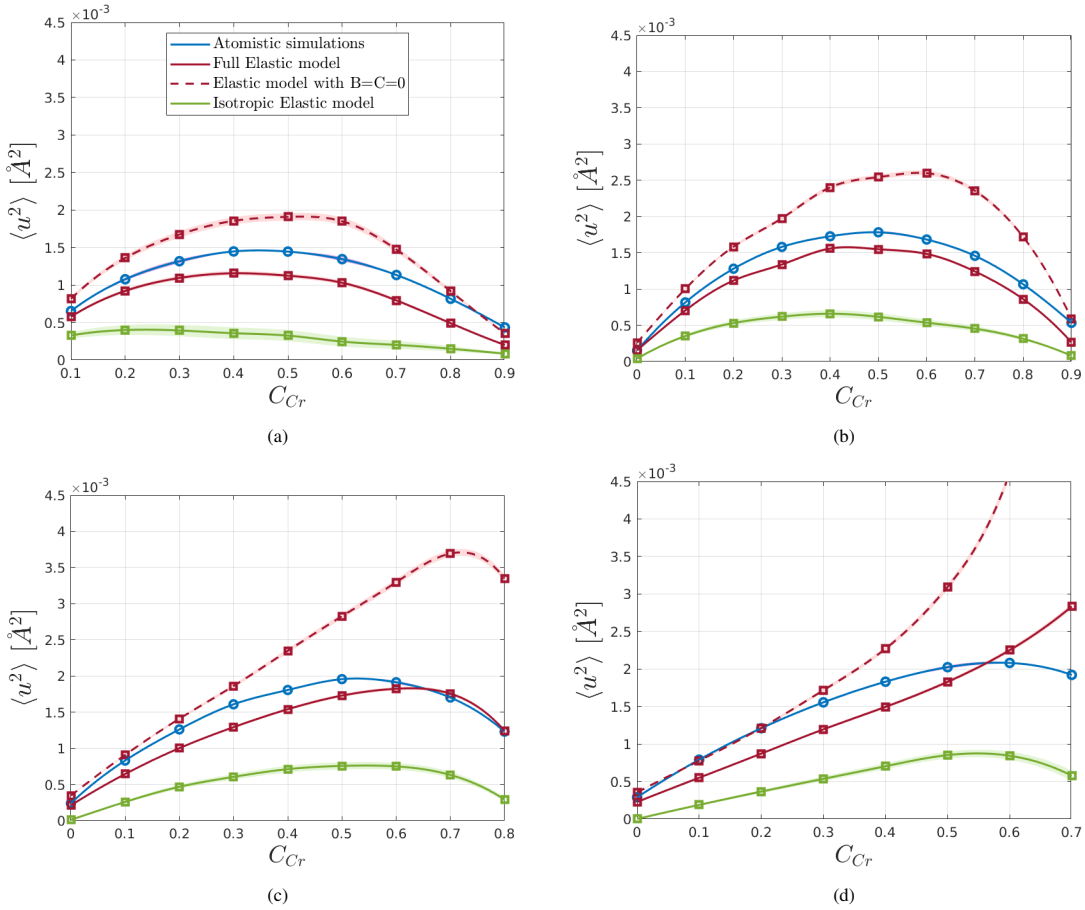

Figure 7: Comparison between the atomistic MSAD (circular symbols) and different versions of the elastic model (square symbols) for FeNiCr alloys with different compositions of Ni: (a) 0% (b) 10% (c) 20% (d) 30%.

4.1. Model potential for a binary alloy

4.1.1. Expression of the potential

The original EAM potential is described by the following potential energy:

$$E(r_1, ..., r_N) = \sum_{i=1}^{N} \left[\sum_{j>i} \Phi_W(r_{ij}) + F_W \left(\sum_{j \neq i} \rho_W(r_{ij}) \right) \right], \tag{33}$$

where $\Phi_W(r)$ is a pair potential between atoms of type W, $\rho_W(r)$ the effective electron density and F_W the embedding function. The modification of the EAM potential is performed by adjusting simultaneously the embedding function and the pair potential with two parameters that we note α_{size} and α_{modulus}. They control respectively the size and the elastic moduli of $\widetilde{W}$ atoms ($\alpha_{\text{size}} = 1$ and $\alpha_{\text{modulus}} = 1$ to recover the original W potential).

Considering the expressions of the elastic constants with EAM potentials [57], the elastic constants can be rescaled by multiplying the total energy, and thus the pair potential and the embedding function, by a factor α_{modulus}. As a consequence, choosing $\alpha_{\text{modulus}} > 1$ (resp. < 1) makes $\widetilde{W}$ stiffer (resp. softer) than W.

To change the size of $\widetilde{W}$ atoms and therefore the associated lattice constant, we can divide all distances by a parameter α_{size}. However, this changes the equilibrium atomic volume, which enters in the expression of the elastic constants. To correct for this effect, both the pair potential and the embedding function need to be multiplied by α_{size}^3. Finally, the EAM potential associated with element $\widetilde{W}$ is described by the following functions:

	C_{11} [GPa]	C_{12} [GPa]	C_{44} [GPa]
Ta	266	158	87
Mo	450	173	125
W	533	205	163
V	232	119	46
Nb	253	133	31

Table 2: Elastic constants of some BCC metals taken from Ref. [59].

$$\begin{aligned}\Phi_{\widetilde{W}}(x) &= \alpha_{\text{size}}^3 \alpha_{\text{modulus}} \Phi_W(x/\alpha_{\text{size}}) \\ \rho_{\widetilde{W}}(x) &= \rho_W(x/\alpha_{\text{size}}) \\ F_{\widetilde{W}}(\rho_{\widetilde{W}}) &= \alpha_{\text{size}}^3 \alpha_{\text{modulus}} F_W(\rho)\end{aligned} \tag{34}$$

The pair interactions between W and $\widetilde{W}$ atoms are set by averaging the parameters α_{size} and α_{modulus}:

$$\Phi_{W-\widetilde{W}}(x) = \bar{\alpha}_{\text{size}}^3 \bar{\alpha}_{\text{modulus}} \Phi_W\left(\frac{x}{\bar{\alpha}_{\text{size}}}\right)$$
$$\text{with} \quad \begin{cases} \bar{\alpha}_{\text{modulus}} = \dfrac{1+\alpha_{\text{modulus}}}{2} \\ \bar{\alpha}_{\text{size}} = \dfrac{1+\alpha_{\text{size}}}{2} \end{cases} \tag{35}$$

We also note that modifying the EAM potential as detailed above results in variations of the cohesion energy of the alloy. In particular, the energy associated with $W-W$, $\widetilde{W}-\widetilde{W}$ and $W-\widetilde{W}$ bounds will be different for $\alpha_{\text{size}}, \alpha_{\text{modulus}} \neq 1$. Therefore implementing a size and/or a modulus mismatch will also introduce different solute-solute interactions in the system, an effect that is not accounted for in our elastic approach.

4.1.2. *Range of variation of the size and elastic moduli mismatches*

For classical alloys, the Hume-Rothery law fixes at 15% the maximum size difference between atoms to allow for crystallization [58]. However, since it has been shown that the Hume-Rothery law breaks down in some BCC HEA [24], we will explore variations of α_{size} from 1 to 1.2.

There is no equivalent of the Hume-Rothery law for the difference in elastic constants. But elastic constants of the pure metals forming concentrated solid solutions can vary greatly, in particular in BCC alloys. For example, Ta-Mo, W-Mo, Ta-Nb, and V-W binary alloys and their mixtures form BCC solid solutions across wide composition and temperature ranges while presenting large contrasts of elastic constants as shown in Tab. 2. To mimic the contrast of elastic constants found in these systems, we will explore variations of $\alpha_{modulus}$ between 1 to 2. This corresponds to an average modulus mismatch parameter (defined in analogy with the size mismatch parameter δ) between 0 and 0.5, the typical range visited by BCC refractory multi-principal element alloys [20].

4.1.3. *Lattice parameter and elastic constants of $W-\widetilde{W}$*

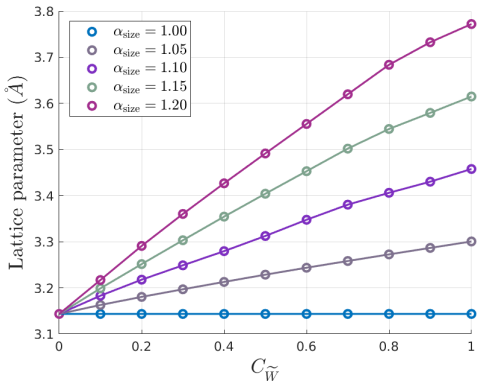

Figure 8: Average lattice parameter of $W-\widetilde{W}$ alloys as a function of the $\widetilde{W}$ concentration with no modulus mismatch ($\alpha_{\text{modulus}} = 1$) and different size mismatches controlled by α_{size}.

To determine the properties of $W-\widetilde{W}$ alloys, we first build a family of binary potentials with no modulus mismatch ($\alpha_{\text{modulus}} = 1$) and a size mismatch between 0% to 20%, i.e. α_{size} from 1 to 1.2. We show in Fig. 8 the average lattice parameter of the random alloys plotted as a function of the concentration of $\widetilde{W}$. These results are obtained after the relaxation of $2,000$-atom cells with the target composition. For reasonable values of $\alpha_{\text{size}} < 1.1$, the lattice constant evolves linearly with the composition, i.e. the alloys follow Vegard's law [60]. A deviation from this linear behavior is obtained for large size mismatches, which is attributed to non-linearities in the interatomic potential that are visited because of atomic displacements induced by the large size contrast.

In a second step, to characterize the effect of α_{modulus} on the elastic constants, we build a family of potentials where α_{modulus} ranges from 1 to 2, in two cases: no size mismatch ($\alpha_{\text{size}} = 1$) and a size mismatch of 5% ($\alpha_{\text{size}} = 1.05$). We show in Fig. 9 the evolution of the average shear modulus as a function of the concentration in $\widetilde{W}$. The reference value for pure W is $\mu_W = 160.9$ GPa, whereas the value obtained for pure $\widetilde{W}$ is by construction given by $\mu_{\widetilde{W}} = \alpha_{\text{modulus}}\mu_W$, with both $\alpha_{\text{size}} = 1.0$ and 1.05. The situation is more complicated in the case of the $W-\widetilde{W}$ alloys: in absence of size mismatch (Fig. 9(a)), the elastic constant increases close

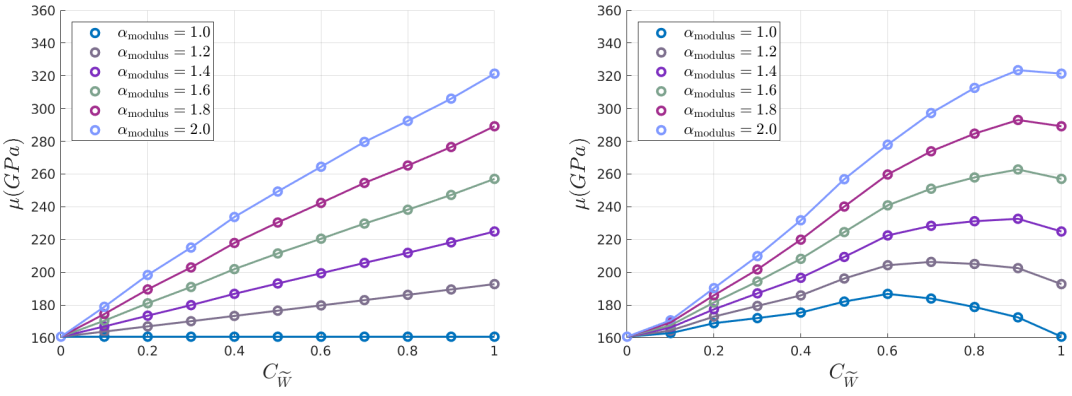

Figure 9: Shear modulus of $W - \widetilde{W}$ alloys as a function of the $\widetilde{W}$ concentration for different modulus mismatches controlled by the α_{modulus} parameter. Two size mismatches are considered: (a) $\alpha_{\text{size}} = 1$ (i.e. no size mismatch) and (b) $\alpha_{\text{size}} = 1.05$.

to linearly with composition, especially for the smaller values of α_{modulus}. When a size mismatch is included (Fig. 9(b)), the elastic modulus no longer varies linearly. This is probably again due to non-linear effects induced by the introduction of both α_{size} and $\alpha_{\text{modulus}} \neq 1$: the atomic displacements resulting from introducing a size mismatch may be affected by the elastic constant of the alloy.

4.2. MSAD with homogeneous elastic constants

We first consider the case of homogeneous elastic constants ($\alpha_{\text{modulus}} = 1$) and investigate the role of α_{size} on the MSAD and how it is reproduced by the elastic model. For different values of α_{size} ranging from 1.01 to 1.075, we compute the elastic constants of the alloy and the parameters A, B, and C of the elastic model as detailed in Section 3.2, employing simulation cells containing $2,000$ atoms populating a BCC lattice. Because the EAM potential for $W - \widetilde{W}$ is built to only include a size misfit, the influence of the terms B and C are negligible as compared to A, which itself is dominated by the size effect and not the fluctuations. Using Vegard's law, the eigenstrains associated to W and $\widetilde{W}$ are expected to be respectively $\varepsilon_W \simeq -c_{\widetilde{W}}(\alpha_{\text{size}} - 1)$ and $\varepsilon_{\widetilde{W}} \simeq (1 - c_{\widetilde{W}})(\alpha_{\text{size}} - 1)$, such that $A \simeq (\alpha_{\text{size}} - 1)^2 c_{\widetilde{W}}(1 - c_{\widetilde{W}})$. For reasonable values of the size misfit $\alpha_{\text{size}} \leq 1.05$, the values of A found numerically fall within 25% of this estimate. The discrepancy increases with the size misfit due to non-linear effects modifying this simple scaling.

As presented in Figs. 10a, 10b and 10c, when the size mismatch is typically $\leq 5\%$, the elastic model predicts accurately the atomistic MSAD. Both follow the parabolic dependence on composition and scale with the square of the size mismatch as expected from Vegard's law. The model slightly overestimates the atomistic MSAD, which could be due to the fact that the parameter α_{size} affects the cohesion energy of the crystal, through the α^3_{size} factor in Eqs. (34-35) and therefore introduces different energies for different types of bonds. Such "chemical" effects might have an additional influence on the MSAD that is not incorporated in the elastic model.

On the other hand, going beyond about 5% of size mismatch, the elastic model underestimates the value of the atomistic MSAD (see Fig. 10d), especially for low contents of $\widetilde{W}$ in the alloy. For high values of the size mismatch, atomic displacements are larger, which might induce non-linearities. In particular, for low contents of $\widetilde{W}$, most bonds are in compression, where these non-linearities are stronger. In the following, to avoid non-linearities, we consider $\alpha_{size} = 1.05$ to probe the influence of the elastic modulus mismatch on the MSAD.

4.3. MSAD with heterogeneous elastic constants

To test the effect of heterogeneous elastic constants on the MSAD, we perform a series of calculations at fixed $\alpha_{\text{size}} = 1.05$ Å^2 with α_{modulus} varying from 1.1 to 2. The elastic constants and the parameters of the elastic model are computed as explained previously. Again, we find that $A \gg B, C$, such that the MSAD estimated with the elastic model is dominated by the size contrast between W and $\widetilde{W}$ atoms.

Fig. 11 displays the MSAD obtained for different values of α_{modulus} from atomistic calculations (blue circles) and from the full elastic model (red squares). In Figs. 11a and 11b, the elasticity mismatch is respectively 10% and 20%, which can be considered as low

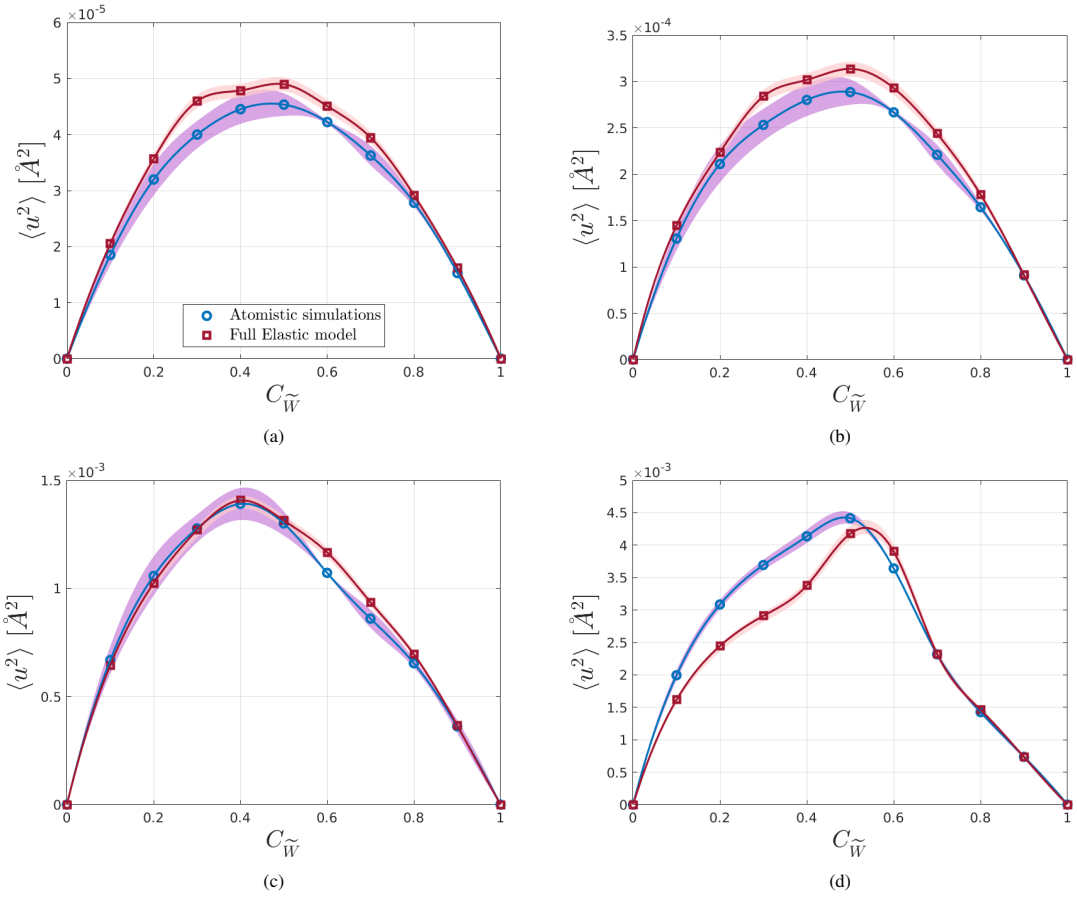

Figure 10: MSAD of $W - \widetilde{W}$ alloys computed using atomistic simulations (blue circles) or the elastic model (red squares) as a function of the $\widetilde{W}$ concentration in W-$\widetilde{W}$ alloys. Different size mismatches are considered: (a) $\alpha_{\text{size}} = 1.01$, (b) 1.025, (c) 1.05, (d) 1.075 with no modulus mismatch ($\alpha_{\text{modulus}} = 1$). Confidence bounds are shown as colored areas.

to moderate. In these cases, the MSAD obtained from atomistic simulations is not much affected, remaining close to the case with only a size mismatch (see Fig. 10c), and the elastic model is in good agreement with the atomistic calculations across the composition range. This comes as a confirmation of the validity of the elastic model for systems presenting low to moderate elastic heterogeneities.

However, we see in Figs. 11c and 11d that when the elastic constant mismatch is 50% or 100%, the MSAD obtained from atomistic calculations increases significantly. It is interesting to note that for $\alpha_{modulus} = 2$, the values of the MSAD are approximately doubled compared to $\alpha_{modulus} = 1$ (see Fig. 10c). This suggests a linear scaling discussed below.

On the other hand, the values of the MSAD obtained from the elastic model do not vary significantly with α_{modulus}: the peak value of the predicted MSAD remains $\langle u^2 \rangle \simeq 1.5 \cdot 10^{-3}$ for all the values of α_{modulus}. Indeed, Eq. (18), derived with the assumption of homogeneous elastic constants, depends on Poisson's ratio ν but not on the shear modulus μ of the average alloy. We find that ν (and therefore the MSAD) depends only weakly on the value of $\alpha_{modulus}$.

5. Discussion and conclusion

5.1. Environment-dependent anisotropic eigenstrains

We introduced an elastic model to estimate the MSAD in concentrated random alloys, by modeling the atoms as Eshelby inclusions embedded in a continuous elastic medium. This kind of elastic framework is at the basis of strengthening models of random concentrated alloys [10, 61, 62]. It is particularly attractive for alloy design since it is computationally inexpensive and allows to screen large compositional domains [63, 64].

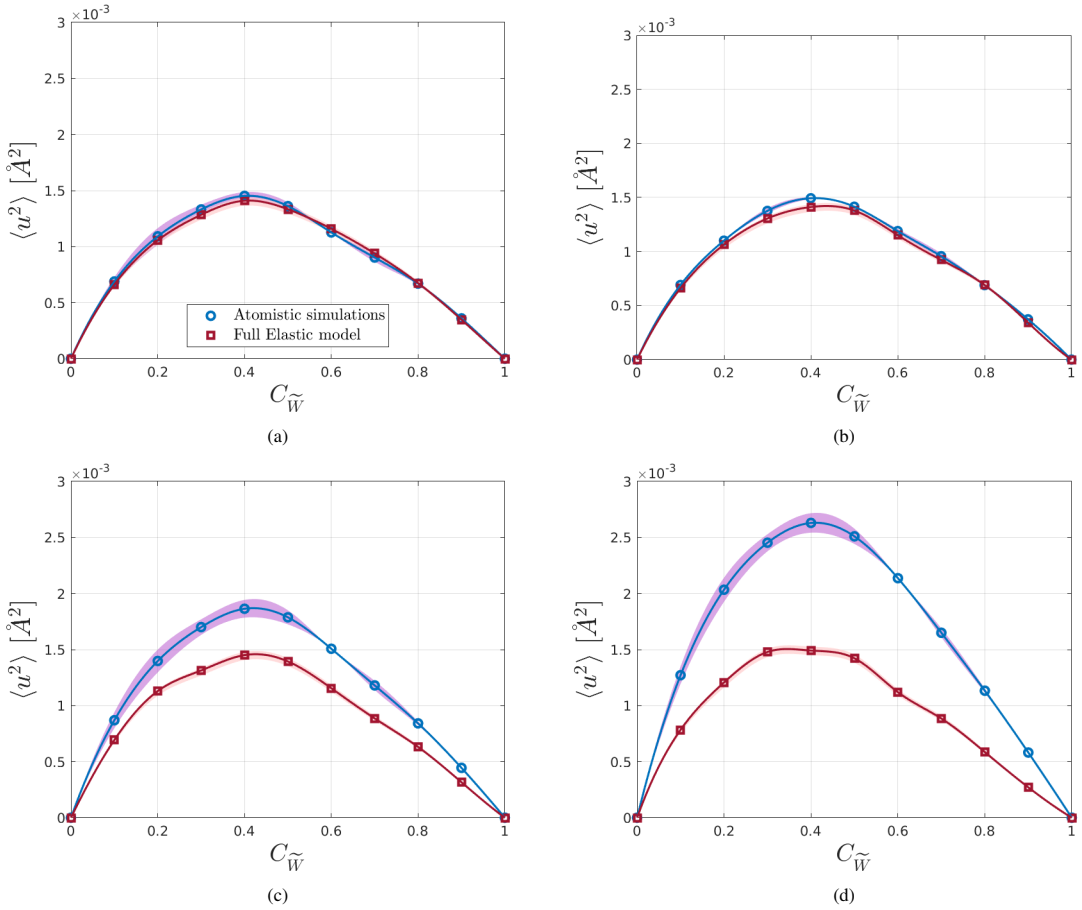

Figure 11: MSAD of $W - \widetilde{W}$ alloys computed using atomistic simulations (blue) or the elastic model (red) as a function of the $\widetilde{W}$ concentration. Different modulus mismatches are considered: (a) $\alpha_{\text{modulus}} = 1.1$, (b) 1.2, (c) 1.5, (d) 2.0 for a given size mismatch ($\alpha_{\text{size}} = 1.05$). Confidence bounds are shown as colored areas.

For this specific goal, atoms of different natures are represented as purely dilatational inclusions and are characterized by a single misfit volume. The same assumptions can be used to yield a simple prediction of the MSAD in concentrated alloys (see Eq. (19)), which has been shown to compare well with atomistic calculations in simple systems such as AlMg alloys [32]. But effects other than a size mismatch can affect the MSAD, as shown here.

We considered in this work the MSAD, which is straightforward to measure atomistically, although one should be careful about cell size effects as illustrated in Fig. 6. Our strategy was to employ the MSAD as a probing tool to assess the assumptions of the elastic model, assuming that the present conclusions also apply to solid solution strengthening since it was shown both experimentally [13] and theoretically [62] that the magnitude of solute strengthening is directly related to the magnitude of the MSAD in random concentrated alloys.

In the present work, we relaxed some assumptions of the initial elastic approach by modeling each atom as an anisotropic eigenstrain tensor that varies depending on the local chemical environment. We obtained an improved prediction of the MSAD of complex alloys. Through a systematic study of a fictitious model, we found that the elastic model predicts accurately the MSAD for size misfits up to about 5 % and elastic modulus misfits up to about 25 %. Moreover, in the case of FeNiCr alloys that have a relatively small size misfit, we have shown that the fluctuations of the atomic eigenstrains with the local environment give rise to the main contribution of the MSAD. Likewise, we expect these fluctuations to play an important role in solute strengthening.

Environment-dependent fluctuations emerge from mixing elements of different natures and cannot be cap-

tured by simplifying the problem and considering atoms embedded in an effective average-atom model [65]. As such, the environmental fluctuations can be seen as a "cocktail effect" emerging from the synergy between the alloy components. This cocktail effect was first mentioned in the seminal literature on high entropy alloys [1, 2, 66] as one of the core effects in high entropy alloys. Its influence on strengthening later became controversial because of the lack of experimental evidence and the success of solid solution models that neglect this contribution [10, 61]. However, there is now clear experimental evidence of wide fluctuations in medium- and high-entropy alloys. In particular, Sohn et al. [67] have shown that replacing Cr with V in an equiatomic CrCoNi alloy not only brings a significant size effect attributed to the large atomic size of V but also introduces larger fluctuations in the bond lengths of Co-Co and Co-Ni and Ni-Ni bonds. Similarly, Tong et al. [23] compared the amplitude of lattice distortions in $Ni_{80}Pd_{20}$ and equiatomic FeCoNiCrPd and revealed the role of "a synergetic effect of chemical complexity" on the wide distribution of atomic bonds in the FeCoNiCrPd HEA. The resulting fluctuations in local lattice distortions may explain why dilute alloys, which do not show fluctuations since solutes mostly see the same matrix environment, have a lower yield strength than HEAs even when they have comparable size mismatch parameters [43, 68].

We note that the strengthening model proposed by Varvenne et al. [10] incorporates the effect of environment-dependent size misfits but neglects their contribution when applying the model to specific systems. The methodology proposed in Section 2.3 offers the possibility to estimate the magnitude of these fluctuations by the means of atomistic calculations. Such simulations are easily performed with classical interatomic potentials and are not out of reach of ab initio calculations as shown in Appendix D. Estimating the magnitude of environment-dependent fluctuations and applying the model of Varvenne et al. [10] would allow to estimate their influence on strengthening, in particular in systems where experimental observations contradict the prediction of elastic models. For example, Thiel et al. [69] have shown that the yield stress of $(AuNiPdPt)_{1-x}$ Cu_x alloys decreases with x while Varvenne's model predicts the opposite if the environment-dependent contribution is neglected.

In addition, using ab-initio calculations would allow to explore more systems and would enable to incorporate additional effects such as magnetism that can play an important role in random alloys [70].

Another strategy to investigate the role of environment-dependent eigenstrains in strengthening is to employ a dislocation dynamics framework. In this context, we plan to investigate the role of these fluctuations on the amplitude and correlations of the stress fields [32, 33] and use these statistical properties to investigate dislocation dynamics in a correlated stress environment [62].

5.2. *Influence of elastic constant mismatch*

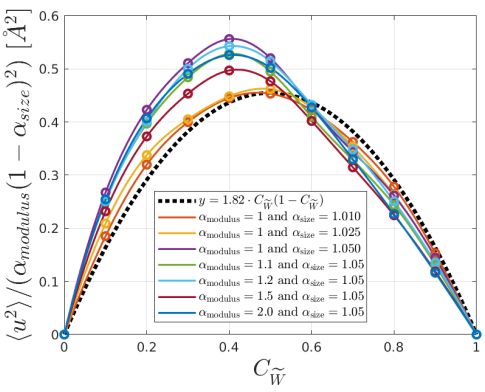

Figure 12: MSAD rescaled by $1/(1-\alpha_{\text{size}})^2\alpha_{\text{modulus}}$, computed using atomistic simulations for different $W - \widetilde{W}$ alloys.

The results discussed in Section 4 show that the contrast of elastic constants between components of an alloy also contributes to the MSAD, although it is not accounted for in elastic models.

It is valuable to investigate the relative effect of both size and modulus mismatch parameters on the MSAD. Fig. 12 displays the atomistic MSAD reported in Fig. 10 and 11 rescaled by the product $(1-\alpha_{size})^2\alpha_{modulus}$. It shows a satisfactory collapse of the data on a master curve of the type $\langle u^2 \rangle \sim (1-\alpha_{size})^2\alpha_{modulus}c_{\widetilde{W}}(1-c_{\widetilde{W}})$ shown with a dashed line. Deviations from this parabolic ideal curve are attributed to non-linear effects emerging when the size parameter $\alpha_{size} \geq 1.05$. As mentioned above, the quadratic scaling with the size mismatch is expected from the elastic model, but the linear scaling with $\alpha_{modulus}$ was rather unexpected and can not be derived from the elastic model presented here.

This scaling can be qualitatively compared with seminal strengthening models. Indeed, the effect of elastic constant mismatch and lattice mismatch was incorporated in the early strengthening models [7, 8] as well as in more recent approaches [9] through an effective misfit parameter $\left(\eta_i^2 + A\delta_i^2\right)^{1/2}$ where $\delta_i = \frac{1}{a_{lat}}\frac{\partial a_{lat}}{\partial c_i}$ and $\eta_i = \frac{1}{\mu}\frac{\partial \mu}{\partial c_i}$ correspond respectively to the size and elastic mismatch contributions and A is a constant generally adjusted on experimental data. The effective misfit

parameter is thus a geometric average of both effects, while the scaling evidenced in Fig. 12 is multiplicative. At this stage, such comparison remains qualitative as the MSAD is only an indirect measure of solid strengthening.

As shown in Section 4, our elastic model does not reproduce the MSAD in alloys with strong misfit contrasts because it relies on an assumption of homogeneous elasticity. Overcoming this limitation appears as desirable as challenging. Indeed, solving for the elastic equilibrium with elastic inclusions and heterogeneities is a non-linear problem [36]. While efficient numerical methods have been developed [36, 55], a close-packed analytical solution to this problem still seems out of reach.

Acknowledgment

The authors acknowledge the support of the French Agence Nationale de la Recherche (ANR), under grant ANR-20-CE08-0019 (project INSPIRA). We gratefully acknowledge support from the CNRS/IN2P3 Computing Center (Lyon - France) for providing computing resources needed for this work. We would also like to thank N.L. Okamoto (IMR, Tohoku University) for fruitful discussions, made possible thanks to GIMRT support for traveling (grant number 202205-RDKGE-0511)

References

[1] D. B. Miracle, O. N. Senkov, A critical review of high entropy alloys and related concepts, Acta Materialia 122 (2017) 448–511.

[2] B. Cantor, Multicomponent high-entropy Cantor alloys, Progress in Materials Science 120 (2021) 100754.

[3] Z. Wu, M. C. Troparevsky, Y. Gao, J. R. Morris, G. M. Stocks, H. Bei, Phase stability, physical properties and strengthening mechanisms of concentrated solid solution alloys, Current Opinion in Solid State and Materials Science 21 (2017) 267–284.

[4] E. P. George, W. Curtin, C. C. Tasan, High entropy alloys: A focused review of mechanical properties and deformation mechanisms, Acta Materialia 188 (2020) 435–474.

[5] F. Zhang, S. Zhao, K. Jin, H. Xue, G. Velisa, H. Bei, R. Huang, J. Ko, D. Pagan, J. Neuefeind, et al., Local structure and short-range order in a NiCoCr solid solution alloy, Physical Review Letters 118 (2017) 205501.

[6] R. Zhang, S. Zhao, J. Ding, Y. Chong, T. Jia, C. Ophus, M. Asta, R. O. Ritchie, A. M. Minor, Short-range order and its impact on the CrCoNi medium-entropy alloy, Nature 581 (2020) 283–287.

[7] R. L. Fleischer, Substitutional solution hardening, Acta Metallurgica 11 (1963) 203–209.

[8] R. Labusch, A statistical theory of solid solution hardening, Physica Status Solidi (B) 41 (1970) 659–669.

[9] I. Toda-Caraballo, P. E. Rivera-Díaz-del Castillo, Modelling solid solution hardening in high entropy alloys, Acta Materialia 85 (2015) 14–23.

[10] C. Varvenne, A. Luque, W. A. Curtin, Theory of strengthening in fcc high entropy alloys, Acta Materialia 118 (2016) 164–176.

[11] Q. He, Y. Yang, On lattice distortions in high entropy alloys, Frontiers in Materials 5 (2018) 42.

[12] H. Ge, F. Tian, A review of ab initio calculation on lattice distortion in high-entropy alloys, JOM 71 (2019) 4225–4237.

[13] N. L. Okamoto, K. Yuge, K. Tanaka, H. Inui, E. P. George, Atomic displacement in the CrMnFeCoNi high-entropy alloy–a scaling factor to predict solid solution strengthening, AIP Advances 6 (2016) 125008.

[14] Y. Zhao, T. Nieh, Correlation between lattice distortion and friction stress in Ni-based equiatomic alloys, Intermetallics 86 (2017) 45–50.

[15] C. Lee, Y. Chou, G. Kim, M. C. Gao, K. An, J. Brechtl, C. Zhang, W. Chen, J. D. Poplawsky, G. Song, et al., Lattice-distortion-enhanced yield strength in a refractory high-entropy alloy, Advanced Materials 32 (2020) 2004029.

[16] B. Chen, S. Li, J. Ding, X. Ding, J. Sun, E. Ma, Correlating dislocation mobility with local lattice distortion in refractory multi-principal element alloys, Scripta Materialia 222 (2023) 115048.

[17] Y. Zhang, Y. J. Zhou, J. P. Lin, G. L. Chen, P. K. Liaw, Solid-solution phase formation rules for multi-component alloys, Advanced Engineering Materials 10 (2008) 534–538.

[18] P. Thirathipviwat, S. Sato, G. Song, J. Bednarcik, K. Nielsch, J. Jung, J. Han, A role of atomic size misfit in lattice distortion and solid solution strengthening of TiNbHfTaZr high entropy alloy system, Scripta Materialia 210 (2022) 114470.

[19] F. G. Coury, M. Kaufman, A. J. Clarke, Solid-solution strengthening in refractory high entropy alloys, Acta Materialia 175 (2019) 66–81.

[20] W. Lai, F. Vogel, X. Zhao, B. Wang, Y. Yi, D. You, X. Tong, W. Li, X. Yu, X. Wang, Design of bcc refractory multi-principal element alloys with superior mechanical properties, Materials Research Letters 10 (2022) 133–140.

[21] H. S. Oh, K. Odbadrakh, Y. Ikeda, S. Mu, F. Körmann, C.-J. Sun, H. S. Ahn, K. N. Yoon, D. Ma, C. C. Tasan, et al., Element-resolved local lattice distortion in complex concentrated alloys: An observable signature of electronic effects, Acta Materialia 216 (2021) 117135.

[22] L. Casillas-Trujillo, B. Osinger, R. Lindblad, D. Karlsson, A. I. Abrikosov, S. Fritze, K. von Fieandt, B. Alling, I. Hotz, U. Jansson, et al., Experimental and theoretical evidence of charge transfer in multi-component alloys–how chemical interactions reduce atomic size mismatch, Materials Chemistry Frontiers 5 (2021) 5746–5759.

[23] Y. Tong, S. Zhao, K. Jin, H. Bei, J. Ko, Y. Zhang, F. Zhang, A comparison study of local lattice distortion in $Ni_{80}Pd_{20}$ binary alloy and FeCoNiCrPd high-entropy alloy, Scripta Materialia 156 (2018) 14–18.

[24] Y. Tong, S. Zhao, H. Bei, T. Egami, Y. Zhang, F. Zhang, Severe local lattice distortion in Zr- and/or Hf-containing refractory multi-principal element alloys, Acta Materialia 183 (2020) 172–181.

[25] Y. Ye, Y. Zhang, Q. He, Y. Zhuang, S. Wang, S. Shi, A. Hu, J. Fan, Y. Yang, Atomic-scale distorted lattice in chemically disordered equimolar complex alloys, Acta Materialia 150 (2018) 182–194.

[26] M. Jafary-Zadeh, K. H. Khoo, R. Laskowski, P. S. Branicio, A. V. Shapeev, Applying a machine learning interatomic potential to unravel the effects of local lattice distortion on the elastic properties of multi-principal element alloys, Journal of Alloys and Compounds 803 (2019) 1054–1062.

[27] S. Mu, R. J. Olsen, B. Dutta, L. Lindsay, G. D. Samolyuk, T. Berlijn, E. D. Specht, K. Jin, H. Bei, T. Hickel, et al., Unfolding the complexity of phonon quasi-particle physics in dis-

ordered materials, NPJ Computational Materials 6 (2020) 1–8.
[28] S. R. Turner, S. Pailhès, F. Bourdarot, J. Ollivier, Y. Sidis, J.-P. Castellan, J.-M. Zanotti, Q. Berrod, F. Porcher, A. Bosak, et al., Phonon behavior in a random solid solution: a lattice dynamics study on the high-entropy alloy FeCoCrMnNi, Nature Communications 13 (2022) 7509.
[29] Y. Ye, C. Liu, Y. Yang, A geometric model for intrinsic residual strain and phase stability in high entropy alloys, Acta Materialia 94 (2015) 152–161.
[30] I. Toda-Caraballo, J. Wróbel, S. Dudarev, D. Nguyen-Manh, P. Rivera-Díaz-del Castillo, Interatomic spacing distribution in multicomponent alloys, Acta Materialia 97 (2015) 156–169.
[31] I. Toda-Caraballo, P. Rivera-Díaz-del Castillo, A criterion for the formation of high entropy alloys based on lattice distortion, Intermetallics 71 (2016) 76–87.
[32] P.-A. Geslin, D. Rodney, Microelasticity model of random alloys. Part I: mean square displacements and stresses, Journal of the Mechanics and Physics of Solids 153 (2021) 104479.
[33] P.-A. Geslin, A. Rida, D. Rodney, Microelasticity model of random alloys. Part II: displacement and stress correlations, Journal of the Mechanics and Physics of Solids 153 (2021) 104480.
[34] J. Eshelby, The continuum theory of lattice defects, in: Solid State Physics, volume 3, Elsevier, 1956, pp. 79–144.
[35] J. D. Eshelby, The determination of the elastic field of an ellipsoidal inclusion, and related problems, Proceedings of the Royal Society of London. Series A. Mathematical and physical sciences 241 (1957) 376–396.
[36] T. Mura, Micromechanics of defects in solids, Springer Netherlands, 1982.
[37] W. G. Nöhring, W. A. Curtin, Correlation of microdistortions with misfit volumes in high entropy alloys, Scripta Materialia 168 (2019) 119–123.
[38] C. Varvenne, G. P. M. Leyson, M. Ghazisaeidi, W. A. Curtin, Solute strengthening in random alloys, Acta Materialia 124 (2017) 660–683.
[39] G. D. Samolyuk, Y. Osetsky, G. M. Stocks, J. Morris, Role of static displacements in stabilizing body centered cubic high entropy alloys, Physical Review Letters 126 (2021) 025501.
[40] A. F. Bower, Applied mechanics of solids, CRC press, 2009.
[41] T. Albaret, A. Tanguy, F. Boioli, D. Rodney, Mapping between atomistic simulations and eshelby inclusions in the shear deformation of an amorphous silicon model, Physical Review E 93 (2016) 053002.
[42] P. Billingsley, Probability and measure, John Wiley & Sons, 2008.
[43] K.-H. Lin, C.-M. Tseng, C.-C. Chueh, S.-Y. Chang, Y.-C. Lo, C.-C. Wang, S.-J. Lin, J.-W. Yeh, Different lattice distortion effects on the tensile properties of Ni-W dilute solutions and CrFeNi and CoCrFeMnNi concentrated solutions, Acta Materialia 221 (2021) 117399.
[44] M. Schneider, G. Laplanche, Effects of temperature on mechanical properties and deformation mechanisms of the equiatomic CrFeNi medium-entropy alloy, Acta Materialia 204 (2021) 116470.
[45] X.-Y. Liu, J. B. Adams, Grain-boundary segregation in Al–10% Mg alloys at hot working temperatures, Acta Materialia 46 (1998) 3467–3476.
[46] G. Bonny, D. Terentyev, R. Pasianot, S. Poncé, A. Bakaev, Interatomic potential to study plasticity in stainless steels: the FeNiCr model alloy, Modelling and Simulation in Materials Science and Engineering 19 (2011) 085008.
[47] S. Plimpton, Fast parallel algorithms for short-range molecular dynamics, Journal of Computational Physics 117 (1995) 1–19.
[48] E. Bitzek, P. Koskinen, F. Gähler, M. Moseler, P. Gumbsch, Structural relaxation made simple, Physical Review Letters 97 (2006) 170201.
[49] R. Scattergood, D. Bacon, The Orowan mechanism in anisotropic crystals, Philosophical Magazine 31 (1975) 179–198.
[50] R. Scattergood, D. Bacon, The strengthening effect of voids, Acta Materialia 30 (1982) 1665–1677.
[51] B. Yin, W. Curtin, First-principles-based prediction of yield strength in the RhIrPdPtNiCu high-entropy alloy, NPJ Computational Materials 5 (2019) 14.
[52] R. B. Sills, M. E. Foster, X. W. Zhou, Line-length-dependent dislocation mobilities in an fcc stainless steel alloy, International Journal of Plasticity 135 (2020) 102791.
[53] C. Lee, G. Song, M. C. Gao, R. Feng, P. Chen, J. Brechtl, Y. Chen, K. An, W. Guo, J. D. Poplawsky, et al., Lattice distortion in a strong and ductile refractory high-entropy alloy, Acta Materialia 160 (2018) 158–172.
[54] G. Kim, H. Diao, C. Lee, A. Samaei, T. Phan, M. de Jong, K. An, D. Ma, P. K. Liaw, W. Chen, First-principles and machine learning predictions of elasticity in severely lattice-distorted high-entropy alloys with experimental validation, Acta Materialia 181 (2019) 124–138.
[55] H. Moulinec, P. Suquet, A numerical method for computing the overall response of nonlinear composites with complex microstructure, Computer Methods in Applied Mechanics and Engineering 157 (1998) 69–94.
[56] M.-C. Marinica, L. Ventelon, M. Gilbert, L. Proville, S. Dudarev, J. Marian, G. Bencteux, F. Willaime, Interatomic potentials for modelling radiation defects and dislocations in tungsten, Journal of Physics: Condensed Matter 25 (2013) 395502.
[57] M. S. Daw, M. I. Baskes, Embedded-atom method: Derivation and application to impurities, surfaces, and other defects in metals, Physical Review B 29 (1984) 6443.
[58] U. Mizutani, The Hume-Rothery rules for structurally complex alloy phases, in: Surface Properties and Engineering of Complex Intermetallics, World Scientific, 2010, pp. 323–399.
[59] P. Söderlind, O. Eriksson, J. Wills, A. Boring, Theory of elastic constants of cubic transition metals and alloys, Physical Review B 48 (1993) 5844.
[60] L. Vegard, Die konstitution der mischkristalle und die raumfüllung der atome, Zeitschrift fur Physik 5 (1921) 17–26.
[61] F. Maresca, W. A. Curtin, Mechanistic origin of high strength in refractory BCC high entropy alloys up to 1900K, Acta Materialia 182 (2020) 235–249.
[62] A. Rida, E. Martinez, D. Rodney, P.-A. Geslin, Influence of stress correlations on dislocation glide in random alloys, Physical Review Materials 6 (2022) 033605.
[63] C. Varvenne, W. A. Curtin, Predicting yield strengths of noble metal high entropy alloys, Scripta Materialia 142 (2018) 92–95.
[64] Y. Rao, C. Baruffi, A. De Luca, C. Leinenbach, W. Curtin, Theory-guided design of high-strength, high-melting point, ductile, low-density, single-phase BCC high entropy alloys, Acta Materialia 237 (2022) 118132.
[65] C. Varvenne, A. Luque, W. G. Nöhring, W. A. Curtin, Average-atom interatomic potential for random alloys, Physical Review B 93 (2016) 104201.
[66] J.-W. Yeh, Recent progress in high entropy alloys, Annales De Chimie - Science des Materiaux 31 (2006) 633–648.
[67] S. S. Sohn, A. Kwiatkowski da Silva, Y. Ikeda, F. Körmann, W. Lu, W. S. Choi, B. Gault, D. Ponge, J. Neugebauer, D. Raabe, Ultrastrong medium-entropy single-phase alloys designed via severe lattice distortion, Advanced Materials 31 (2019) 1807142.
[68] S. Yoshida, T. Ikeuchi, T. Bhattacharjee, Y. Bai, A. Shibata, N. Tsuji, Effect of elemental combination on friction stress and hall-petch relationship in face-centered cubic high/medium en-

tropy alloys, Acta Materialia 171 (2019) 201–215.
[69] F. Thiel, D. Utt, A. Kauffmann, K. Nielsch, K. Albe, M. Heilmaier, J. Freudenberger, Breakdown of varvenne scaling in $(AuNiPdPt)_{1-x}$ Cu_x high-entropy alloys, Scripta Materialia 181 (2020) 15–18.
[70] J. Wróbel, M. Zemła, D. Nguyen-Manh, P. Olsson, L. Messina, C. Domain, T. Wejrzanowski, S. Dudarev, Elastic dipole tensors and relaxation volumes of point defects in concentrated random magnetic Fe-Cr alloys, Computational Materials Science 194 (2021) 110435.

Appendices

Appendix A. Displacement field outside an inclusion

The elastic displacement field $\boldsymbol{u}(\boldsymbol{r}) = [u_1(\boldsymbol{r}), u_2(\boldsymbol{r}), u_3(\boldsymbol{r})]$ outside a spherical inclusion characterized by an eigenstrain tensor $[\varepsilon_1^\alpha, \ldots, \varepsilon_6^\alpha]$ can be written as the sum:

$$u_k(\boldsymbol{r}) = \sum_i^6 \varepsilon_i^\alpha f_{ik}(\boldsymbol{r}) \tag{A.1}$$

where the elastic functions $f_{ik}(\boldsymbol{r}) = f_{ik}(x, y, z)$ can be found in Ref. [35, 40] and are reported below:

$$f_{11} = \frac{3v_{at}x}{8\pi(1-\nu)}\left(-\frac{a^2x^2}{R^7} + \frac{3a^2+5x^2}{5R^5} + \frac{(1-2\nu)}{3R^3}\right)$$

$$f_{21} = \frac{3v_{at}x}{8\pi(1-\nu)}\left(\frac{-a^2y^2}{R^7} + \frac{a^2+5y^2}{5R^5} - \frac{(1-2\nu)}{3R^3}\right)$$

$$f_{31} = \frac{3v_{at}x}{8\pi(1-\nu)}\left(\frac{-a^2z^2}{R^7} + \frac{a^2+5z^2}{5R^5} - \frac{(1-2\nu)}{3R^3}\right)$$

$$f_{41} = \frac{3v_{at}xyz}{4\pi(1-\nu)}\left(\frac{1}{R^5} - \frac{a^2}{R^7}\right) \tag{A.2}$$

$$f_{51} = \frac{3v_{at}z}{4\pi(1-\nu)}\Big(\frac{1}{15R^5}(3a^2-5R^2) + \frac{x^2}{R^7}(R^2-a^2) + \frac{2(1-\nu)}{3R^3}\Big)$$

$$f_{61} = \frac{3v_{at}y}{4\pi(1-\nu)}\Big(\frac{1}{15R^5}(3a^2-5R^2) + \frac{x^2}{R^7}(R^2-a^2) + \frac{2(1-\nu)}{3R^3}\Big),$$

with

$$R^2 = x^2 + y^2 + z^2$$

Elastic functions $f_{i2}(x, y, z)$ and $f_{i3}(x, y, z)$ are obtained by circular permutations.

Appendix B. Displacement field around a solute atom.

To assess the validity of the elastic description of atomistic systems, we compare the displacements around a misfitting solute atom with the elastic analytical solution. For simplicity, we focus on the W-$\widetilde{W}$ system introduced in section 4 where $\widetilde{W}$ atoms are characterized by a positive volume misfit with respect to W. In particular, different values of α_{size} (α_{size} = 1.01, 1.025 and 1.05) corresponding to different atomic volume misfits between the components of the alloy, were considered while we used $\alpha_{\text{modulus}} = 1$ to maintain the same elastic constants between W and $\widetilde{W}$. A $\widetilde{W}$ atom is introduced in a large cubic cell containing 432000 W atoms. The atomic system is then relaxed following the procedure described in section 3.1. The atomic displacements around the $\widetilde{W}$ atom can be compared to the elastic solution detailed in Appendix A. Because of the symmetry of the simulation cell, the eigenstrain tensor characterizing the $\widetilde{W}$ atom is necessarily diagonal and characterised by a dilatational eigenstrain denoted ε. The displacement field around such inclusion is radial and reduces to:

$$u(r) = \varepsilon \frac{v_{at}}{4\pi}\frac{1+\nu}{1-\nu}\frac{1}{r^2} \tag{B.1}$$

Fig. B.13 compares the atomic displacements obtained from atomistic calculations with the analytical solution of Eq. (B.1). For the different values of α_{size}, the atomistic displacements match well the analytical solution, especially at long-range. The differences obtained for short distances can be explained by the non-linearities of the interatomic potential and by the discrete nature of the atomic lattice, that contrasts with the isotropic elastic medium considered in the elastic model.

Appendix C. Geometrical sums for BCC and FCC lattices

The expression of the MSAD in Section 2.2 involves geometrical sums that need to be computed numerically. We provide below their values for BCC and FCC lattices in the limit of infinite systems. For a BCC lattice with distances scaled by the lattice parameter, we have:

$$\sum_{n=1}^{N}\frac{1}{R_n^4} \approx 40.25 \quad \sum_{n=1}^{N}\frac{1}{R_n^6} \approx 29.05 \quad \sum_{n=1}^{N}\frac{1}{R_n^8} \approx 32.73 \tag{C.1}$$

$$\sum_{n=1}^{N}\frac{R_n'^4}{R_n^8} \approx 8.847 \quad \sum_{n=1}^{N}\frac{R_n'^4}{R_n^{10}} \approx 7.193 \quad \sum_{n=1}^{N}\frac{R_n'^4}{R_n^{12}} \approx 8.747$$

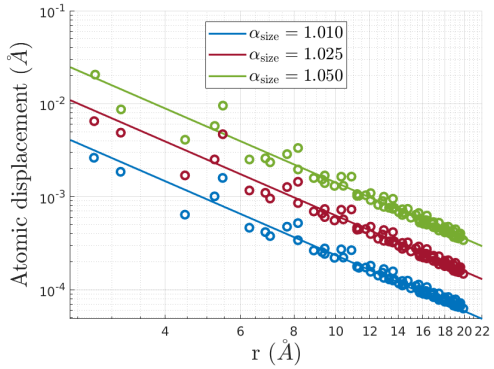

Figure B.13: Atomic displacements around an isolated $\widetilde{W}$ atom in a W crystal with different choices of volume misfit. The continuous lines represent the analytical elastic solution.

with $R_n'^4$ defined by:

$$R_n'^4 = x_n^2 y_n^2 + x_n^2 z_n^2 + y_n^2 z_n^2 \tag{C.2}$$

For a FCC lattice:

$$\sum_{n=1}^{N} \frac{1}{R_n^4} \approx 101.4 \qquad \sum_{n=1}^{N} \frac{1}{R_n^6} \approx 115.6 \qquad \sum_{n=1}^{N} \frac{1}{R_n^8} \approx 204.8 \tag{C.3}$$

$$\sum_{n=1}^{N} \frac{R_n'^4}{R_n^8} \approx 21.92 \qquad \sum_{n=1}^{N} \frac{R_n'^4}{R_n^{10}} \approx 27.05 \qquad \sum_{n=1}^{N} \frac{R_n'^4}{R_n^{12}} \approx 49.59$$

Appendix D. Convergence of A, B, and C with cell size

From Section 2.3.2, we expect that the relative error on the terms A, B, and C should not depend on the system size. We checked this through direct atomistic calculations in the case of equiatomic FeNiCr. The result is shown in Fig. D.14 from 4,000 cubic simulation cells of different sizes.

The use of a 32-atom cell ($2 \times 2 \times 2$ cubic unit cells) constrains the second-nearest neighbors because of the periodic boundary conditions. Therefore, it does not allow for the exploration of all the possible neighboring environments and results in biased estimates of A, B, and C.

For cells containing at least 108 atoms, the estimated values of A, B, and C correspond to the limit for large cells, and no significant size effect is observed. It also shows that estimating A, B and C is not out of reach of *ab initio* calculations: performing 100 simulations containing 108-atoms and making use of symmetry arguments would enable to compute A, B, and C with an acceptable uncertainty.

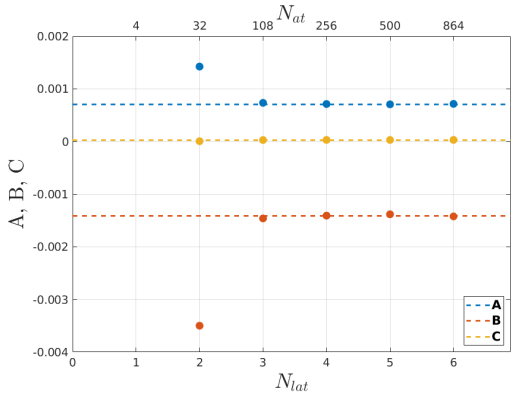

Figure D.14: Convergence of the A, B, C terms with simulation cell size for an equiatomic FeNiCr alloy. The cell size is expressed as a function of the number of atoms (N_{at}) (top horizontal axis) and the number of unit cells along a side of the cubic cells (N_{lat}) (bottom horizontal axis). The error bars associated to the standard error on A,B and C are smaller than the symbol size. The dashed lines are the values obtained in large simulation cells containing 4,000 atoms.